

ExoMiner++ on TESS with Transfer Learning from Kepler: Transit Classification and Vetting Catalog for 2-min Data

HAMED VALIZADEGAN,^{1,2} MIGUEL J. S. MARTINHO,^{1,2} JON M. JENKINS,² JOSEPH D. TWICKEN,^{3,2}
DOUGLAS A. CALDWELL,^{3,2} PATRICK MAYNARD,⁴ HONGBO WEI,⁵ WILLIAM ZHONG,⁶ CHARLES YATES,⁵ SAM DONALD,⁷
KAREN A. COLLINS,⁸ DAVID LATHAM,⁸ KHALID BARKAOUI,^{9,10,11} PERRY BERLIND,⁸ MICHAEL L. CALKINS,⁸
KYLEE CARDEN,¹² NIKITA CHAZOV,¹³ GILBERT A. ESQUERDO,⁸ TRISTAN GUILLOT,¹⁴ VADIM KRUSHINSKY,¹⁵
GRZEGORZ NOWAK,¹⁶ BENJAMIN V. RACKHAM,^{17,18} AMAURY TRIAUD,¹⁹ RICHARD P. SCHWARZ,⁸ DENISE STEPHENS,²⁰
CHRIS STOCKDALE,²¹ JIAQI WANG,²² CRISTILYN N. WATKINS,⁸ AND FRANCIS P. WILKIN²³

¹*Universities Space Research Association (USRA), Mountain View, CA 94043, USA*

²*NASA Ames Research Center (NASA ARC), Moffett Field, CA 94035, USA*

³*The SETI Institute, Mountain View, CA 94043, USA*

⁴*NASA Goddard Space Flight Center, Greenbelt, MD 20771, USA**

⁵*University of California, Berkeley, Berkeley, CA 94720, USA**

⁶*Yale University, New Haven, CT 06520, USA**

⁷*Pacific Northwest National Laboratory, Richland, WA 99354, USA†*

⁸*Center for Astrophysics | Harvard & Smithsonian, 60 Garden Street, Cambridge, MA 02138, USA*

⁹*Astrobiology Research Unit, Université de Liège, 19C Allée du 6 Août, 4000 Liège, Belgium*

¹⁰*Department of Earth, Atmospheric and Planetary Science, Massachusetts Institute of Technology, 77 Massachusetts Avenue, Cambridge, MA 02139, USA*

¹¹*Instituto de Astrofísica de Canarias (IAC), Calle Vía Láctea s/n, 38200, La Laguna, Tenerife, Spain*

¹²*Department of Astronomy, The Ohio State University, 140 West 18th Ave., Columbus, OH 43210 USA*

¹³*Kourovka observatory | Ural Federal University, 19 Mira street, Yekaterinburg, 620002, Russia*

¹⁴*Observatoire de la Côte d'Azur, UniCA, Laboratoire Lagrange, CNRS UMR 7293, CS 34229, 06304 Nice cedex 4, France*

¹⁵*Laboratory of Astrochemical Research | Ural Federal University, ul. Mira d. 19, Yekaterinburg, 620002, Russia*

¹⁶*Institute of Astronomy, Faculty of Physics, Astronomy and Informatics, Nicolaus Copernicus University, Grudziądzka 5, 87-100 Toruń, Poland*

¹⁷*Department of Earth, Atmospheric and Planetary Sciences, Massachusetts Institute of Technology, 77 Massachusetts Avenue, Cambridge, MA 02139, USA*

¹⁸*Kavli Institute for Astrophysics and Space Research, Massachusetts Institute of Technology, Cambridge, MA 02139, USA*

¹⁹*School of Physics & Astronomy, University of Birmingham, Edgbaston, Birmingham, B15 2TT, UK*

²⁰*Department of Physics and Astronomy, Brigham Young University, N-486 ESC, Provo, UT 84602 USA*

²¹*Hazelwood Observatory, Australia*

²²*CAS Key Laboratory of Optical Astronomy, National Astronomical Observatories, Chinese Academy of Sciences, Beijing 100101, China*

²³*Department of Physics and Astronomy, Union College, 807 Union St., Schenectady, NY 12308, USA*

Submitted to AJ

ABSTRACT

We present **ExoMiner++**, an enhanced deep learning model that builds on the success of **ExoMiner** (Valizadegan et al. 2022) to improve transit signal classification in 2-minute TESS data. **ExoMiner++** incorporates additional diagnostic inputs, including periodogram, flux trend, difference image, unfolded flux, and spacecraft attitude control data, all of which are crucial for effectively distinguishing transit signals from more challenging sources of false positives. To further enhance performance, we leverage transfer learning from high-quality labeled data from the Kepler space telescope, mitigating the impact of TESS's noisier and more ambiguous labels. **ExoMiner++** achieves high accuracy across various classification and ranking metrics, significantly narrowing the search space for follow-up investigations

Corresponding author: Hamed Valizadegan

hamed.valizadegan@nasa.gov

to confirm new planets. To serve the exoplanet community, we introduce new TESS catalog containing **ExoMiner++** classifications and confidence scores for each transit signal. Among the 147,568 unlabeled TCEs, **ExoMiner++** identifies 7,330 as planet candidates, with the remainder classified as false positives. These 7,330 planet candidates correspond to 1,868 existing TESS Objects of Interest (TOIs), 69 Community TESS Objects of Interest (CTOIs), and 50 newly introduced CTOIs. 1,797 out of the 2,506 TOIs previously labeled as planet candidates in ExoFOP are classified as planet candidates by **ExoMiner++**. This reduction in plausible candidates combined with the excellent ranking quality of **ExoMiner++** allows the follow-up efforts to be focused on the most likely candidates, increasing the overall planet yield.

1. INTRODUCTION

The discovery and characterization of exoplanets have significantly expanded our understanding of planetary systems beyond the solar system. Among the primary methods for detecting these distant worlds is the transit method, which measures periodic dips in stellar brightness caused by an exoplanet crossing in front of its host star. This method provides crucial data on the exoplanet’s radius, orbital parameters, and can even offer constraints on atmospheric properties. NASA’s Kepler Space Telescope (Borucki et al. 2010) and the Transiting Exoplanet Survey Satellite (TESS; Ricker et al. 2015), launched in 2009 and 2018 respectively, have been instrumental in advancing transit-based exoplanet research, providing large volumes of high-precision photometric data.

Comparing Kepler and TESS reveals divergent observational approaches reflecting distinct missions within the exoplanetary exploration landscape. Kepler pointed at a single field of stars, yielding a comprehensive dataset for statistical analyses, while TESS, through a dynamic all-sky survey, targeted bright and nearby stars for potential exoplanet discoveries, marking a shift from a deep, narrow-field survey to a broader, shallower one. The unique characteristics of TESS data, including challenges posed by its geocentric orbit and observation cadence, demand advanced techniques for precise transit signal extraction. Navigating these complexities is crucial for realizing the scientific potential in TESS’s expansive dataset, underscoring the ongoing commitment to refining methodologies in unraveling exoplanetary intricacies.

Furthermore, TESS’s brief target observations pose a distinctive challenge for transit signal disposition, especially when contrasted with Kepler’s prolonged observations. TESS’s strategy of scanning the entire sky in roughly 27-day segments results in shorter windows of observation for individual stars, introducing period aliasing (especially for multi-transiting planet systems),

and impacting the signal-to-noise ratio (SNR), making it more challenging to distinguish genuine planetary signals from instrumental noise or other astrophysical phenomena. Meticulous data analysis, employing advanced cotrending methods and systematic effects mitigation, becomes imperative to extract reliable information from TESS’s comparatively shorter light curves (Twicken et al. 2020). Despite these challenges, TESS’s unique observational approach offers valuable insights into more diverse celestial objects than studies by Kepler, necessitating tailored strategies to unlock the full potential of its rich yet temporally constrained dataset.

The volume and complexity of TESS data demand advanced analytical tools, with machine learning (ML), particularly deep learning techniques, emerging as crucial tools. Periodic transit-like features in light curves, called Threshold Crossing Events (TCEs), are automatically identified in TESS or Kepler data by the Science Processing Operations Center (SPOC; Jenkins et al. 2016) pipeline. However, not all TCEs are indicative of planets; many are false positives requiring further analysis. The task of classifying transit signals, which is the main focus of this work, involves distinguishing between signals attributable to planets and those arising from various false positive sources (Sullivan et al. 2015). Different machine learning classifier technologies have been employed for this task, including Random Forest (McCauliff et al. 2015; Armstrong et al. 2020), Gaussian Processes (Armstrong et al. 2020), Deep Neural Networks (Valizadegan et al. 2022; Shallue & Vanderburg 2018; Ansdell et al. 2018; Yu et al. 2019; Tey et al. 2023; Salinas et al. 2023), Logistic Regression (Valizadegan et al. 2023), and others.

Previous work (Valizadegan et al. 2022, 2023; Armstrong et al. 2020; Shallue & Vanderburg 2018; Ansdell et al. 2018; Osborn et al. 2020; Tey et al. 2023; Yu et al. 2019) has demonstrated the efficacy of ML methods in analyzing TCEs for telescopes like Kepler or TESS. These models automate the classification of TCEs, streamlining the analysis pipeline and reducing the need for manual inspection. Beyond classification, machine learning approaches have been applied to validation (Armstrong et al. 2020; Valizadegan et al. 2022, 2023; Tey et al. 2023)

* Author contributed while interning at NASA ARC

† Author contributed while interning at NASA through *I*² program

and detection (Cui et al. 2021; Hansen & Dittmann 2024) of transit signals. These methods play a crucial role in the validation of new exoplanets, particularly for TESS, where the mission has yielded a limited number of confirmed planet (CP) discoveries after six years.

Recent works, such as **ExoMiner** (Valizadegan et al. 2022), our previous CNN model, have made significant advancements by incorporating numerous diagnostic tests as inputs and validating hundreds of new exoplanets. Our present work represents a natural extension and adaptation of the successful **ExoMiner** model to the TESS dataset. By leveraging the lessons learned from Kepler and incorporating them into the TESS framework, we aim to enhance the efficiency and accuracy of transit signal classification. For the first time, we include four new diagnostic tests as inputs to the model: difference image, flux trend, flux periodogram, and spacecraft reaction wheel desaturation event (“momentum dump”) data. These tests have proved crucial for human vetting and may prove useful for machine classification of transit signals but have seldom been adopted for machine use due to their complexity. This work not only refines the transit signal classification process for TESS, addressing its unique observational challenges, but also sets the stage for applying these methodologies to future transit surveys.

This paper is organized as follows: Section 2 introduces a general framework for machine learning classification of transit signals, discussing how existing and future classifiers can be viewed as specific instances of this framework. In Section 3, we present **ExoMiner++** as a concrete implementation of this framework. Section 4 details the dataset used in this study and describes the data processing pipeline employed to prepare the inputs for **ExoMiner++**. The hyper-parameter optimization (HPO) process used to tune the parameters of **ExoMiner++** is covered in Section 5. Section 6 evaluates the classification and ranking performance of **ExoMiner++**, using its performance on Kepler as a baseline. Given that the model performs better on Kepler data, Section 6.7 explores the challenges that make the classification of TESS transit signals more difficult compared to those of Kepler. Section 7 presents the **ExoMiner++** catalog, including labels and confidence scores for all TCEs and their corresponding TOIs. Finally, we present our conclusions in Section 8.

2. MACHINE LEARNING CLASSIFICATION OF TRANSIT SIGNALS

We developed **ExoMiner** (Valizadegan et al. 2022) based on the observation that domain experts rely on various components of the Kepler and TESS Data Valida-

tion (DV; Twicken et al. 2018a; Li et al. 2019) reports to classify transit signals. We posited that an effective ML model should be guided by this expert-driven process. DV reports contain a series of diagnostic tests designed to identify different types of false positives (FPs), which are essential inputs for any ML model tasked with transit signal classification. Because **ExoMiner** is a sophisticated deep learning model, it may be challenging for domain experts to fully interpret its decision-making process. In this section, we offer a high-level overview of how machine learning systems, informed by domain expertise, should be structured in general. We then explain how **ExoMiner** follows such structural design.

To design a system capable of vetting a transit signal, it is necessary to process various types of data represented in the DV report, which include: 1) transit-view of the unfolded flux time series, 2) transit-view of the phase-folded flux time series, 3) full-orbit-view of the phase-folded flux time series, 4) transit-view of the phase-folded odd and even flux time series, 5) transit-view of the phase-folded weak secondary flux time series, 6) transit-view of the phase-folded flux-weighted centroid motion time series, 7) difference image, 8) transit-view of the phase-folded momentum dump time series, and 9) several other scalar values such as stellar parameters and DV tests.

The first step in using complex diagnostic inputs, such as time series and images, is to extract features that can discriminate between the classes of interest. This can be done manually by subject matter experts (SMEs) or automatically through a data-driven approach. For example, to extract features from the transit-view of diagnostic tests such as the phase-folded flux, one might use a limb-darkened transit fit model (Mandel & Agol 2002). To determine whether the odd and even test indicates a false positive scenario, one can estimate the transit depth again from a transit fit model and test whether the difference in transit depth between odd and even transits is statistically significant. Once the features/statistics/parameters are extracted and represented as scalar values for different diagnostic tests, they can be combined to classify the transit signals.

Figure 1 shows our proposed architecture, demonstrating a general process that can be used to classify transit signals. As enumerated in the previous paragraph, this system has different diagnostic tests¹ as its input. It consists of five main building blocks to process different diagnostic tests and perform classification, discussed below:

¹ A DV report does not include the periodogram but includes flux before de-trending.

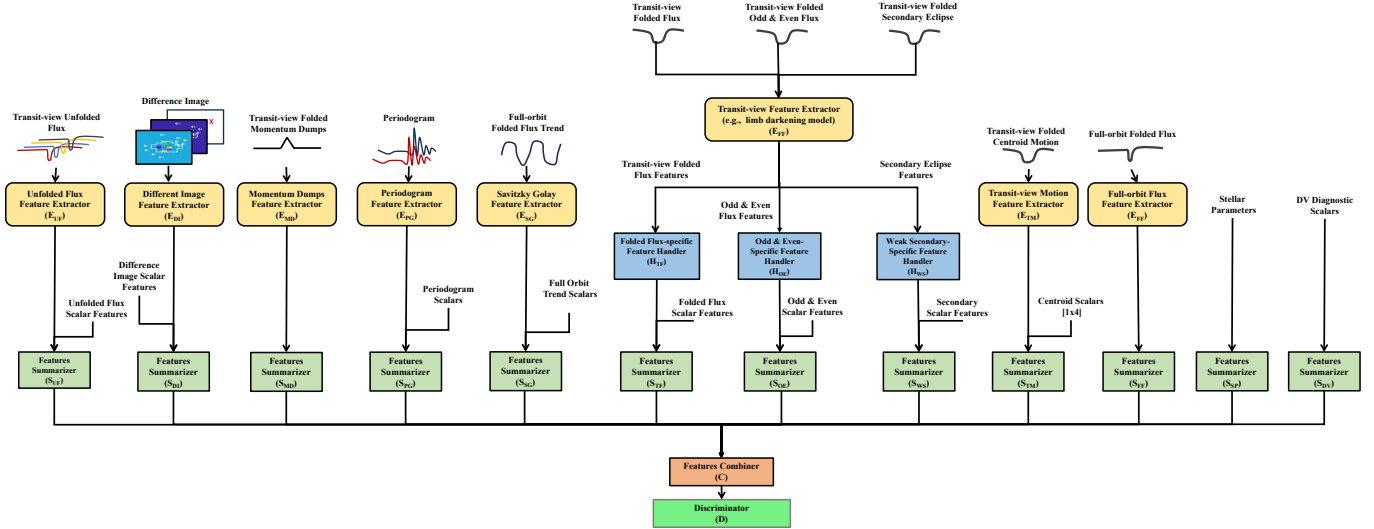


Figure 1. Classification Architecture.

1. **Feature extractor:** This building block is necessary to extract features from complex data types such as images and time series. Different diagnostic tests may require their own specific feature extractors; however, diagnostic types of the same kind might benefit from shared feature extractors. In our model, transit-view of unfolded flux, difference image, transit-view of phase-folded centroid motion time series, full-orbit-view of phase-folded flux, and transit-view of phase-folded momentum dump each have their own feature extractor model. Conversely, the transit-view of phase-folded flux, weak secondary, and odd & even time series share the same feature extractor because we are interested in the characteristics of the transit for these three diagnostic tests. We will discuss this choice in more detail later in Section 3.
2. **Test-specific feature handling:** This component processes features extracted for specific diagnostic tests if special treatment is required. This is only done for transit-view of phase-folded flux, weak secondary, and odd & even time series that share the same feature extractor. For example, after estimating parameters such as transit depth using a limb-darkened transit fit model for odd and even separately, we need to subtract them to determine whether they are statistically different or not.
3. **Feature summarization:** This component summarizes the features extracted by the feature extractor block. This is necessary to obtain more complex features on top of those obtained from the feature extractor block and provides a way to combine relevant scalar values with features extracted from com-

plex data types such as time series or images. For example, in the presence of a weak secondary transit, we need to know whether it is due to an eclipsing binary (EB) star or a large exoplanet exhibiting thermal emission, Doppler boosting, and/or ellipsoidal variations. The feature summarization component combines the features extracted from the weak secondary test with scalar values such as the secondary geometric albedo and planet effective temperature comparison statistics (Twicken et al. 2018a; Jenkins 2020), and other required variables to build the final features for this test.

4. **Feature Combiner:** This component receives the features summarized by the feature summarizers of various diagnostic tests and identifies any high-level complex relationships (linear or nonlinear) between features. It generates a series of final features in which the two classes of interest (exoplanet or false positive) are linearly separable. This component could be a simple model such as principal component analysis (PCA; Jolliffe & Cadima 2016) or a more complex model such as a neural network with millions of parameters (Krizhevsky et al. 2012).
5. **Classification:** This could be a simple linear classifier that receives the highly discriminating features from the previous component and differentiates between the two or more classes of interest.

Traditionally, the feature extraction and the classification were done separately: 1) a pool of feature candidates (i.e., diagnostic tests and their statistics) are proposed by SMEs or extracted by automated features extractors (designed by the data engineers) and 2) a classifier is

designed on top of the extracted features to discriminate the classes of interest. However, these two steps are highly connected. Not only does the discriminating power of the extracted features dictate the kind of classifier we use but also more effective features can be designed by having the type of classifier in mind.

Theoretically, Bayesian classifiers such as **vespa** (Morton et al. 2016) and **TRICERATOPS** (Giacalone et al. 2020) that decompose the posterior into prior and likelihood are optimal (Bishop 2006) for a provided set of independent input variables. However, Bayesian classifiers are difficult to utilize because: 1) they are highly dependent on the assumptions made about the data, which includes accuracy of the priors, the form of likelihood (e.g., Gaussian), and/or independence of features and 2) they cannot be employed when the number of features is more than a few unless we make hard assumptions about the data. Because of this, the classification task in machine learning is concerned with building more flexible classifiers that make fewer assumptions about the data and that are prone to the curse of dimensionality. The efforts in finding such classifiers led to the invention of discriminative classifiers that, unlike Bayesian classifiers, do not decompose the posterior into prior and likelihood, rather they directly optimize the posterior. The compelling justification for solving directly for the posterior given by Vapnik (1998) was that “When solving a problem of interest, do not solve a more general problem as an intermediate step. Try to get the answer that you really need but not a more general one.” The idea is that for the task of classification, we are interested in finding a good decision boundary for which there is no need for a classifier able to generate examples (thus generative model). This idea led to the invention of highly accurate classifiers such as Support Vector Machines (SVMs; Vapnik 1998), Random Forest (Breiman 2001), and Gradient Boosting (Schapire 1990). However, these classifiers still assume the decoupling of the feature extraction and the final task of classification.

To optimize both the feature extraction and classification simultaneously, one can assume a parametric functional form for each component of the architecture in Figure 1. This leads to a huge nested functional form with the outermost function D and innermost functions E , as referred in this figure. After defining an objective function (e.g., a surrogate continuous version for the error rate), one can aim to optimize the parameters of this complex nested function using a set of input/output pairs (training set) to automate the whole process of extracting features to the classification.

Until the invention of the backpropagation algorithm (Schmidhuber 2022), optimizing such complex

nested architectures was a significant challenge. The optimal output (the ground truth in the training set) exists only for the final output of the architecture, not for internal components, such as feature extractors. Backpropagation utilizes the chain rule to propagate the gradient from the final output backward through the network. By assuming a parametric functional form for each component of the model in Figure 1, we can optimize the entire model, including feature extraction and classification, simultaneously. This is the magic behind the tremendous success of deep learning models.

The final consideration is the form of the parametric function for each component. Neural network layers provide one approach, supported by the Universal Approximation Theorem (Hornik et al. 1989), which ensures that a neural network with at least one hidden layer can approximate any function to an arbitrary degree of accuracy, given sufficient units. Different types of neural network layers can also be applied to each component. We will discuss this further in Section 3.1.

2.1. Existing Classifiers

In this section, we demonstrate how the general architecture (or its minor variation) introduced in Section 2 includes the existing machine classifiers. Existing classifiers are different in two major ways: 1) the inclusion of different diagnostic tests represented by different branches and 2) the implementation of different components of this architecture. For example, while some models such as deep learning based classifiers do feature extraction and classification simultaneously, other classifiers assume that such features are already extracted before doing the task of classification. Table 1 demonstrates this difference. If the underlying function is not a deep neural network, a separate feature extractor needs to be employed a-priori before the classification is done; the approach employed by most existing exoplanet transit signal classifiers (Coughlin 2017; Jenkins et al. 2014; McCauliff et al. 2015; Armstrong et al. 2020; Morton et al. 2016; Giacalone et al. 2020). These classifiers differ in the type of functions they employ for the classification which includes expert system if-then rules (Coughlin 2017), random forest (McCauliff et al. 2015; Armstrong et al. 2020), and Bayesian classifiers (Morton et al. 2016; Giacalone et al. 2020).

As shown in Table 1, the existing classifiers also differ in the range of diagnostic tests they use.

3. EXOMINER++

Here we present **ExoMiner++**, an enhanced version of **ExoMiner** with multiple improvements over the original model. **ExoMiner++** incorporates additional data

Table 1. Comparison of different models. * means that the model uses the input diagnostic test directly. † means that the model uses extracted features (i.e., statistics and other parameters) in the form of scalar values from the diagnostic test.

	vespa	Robovetter	Autovetter	AstroNet-2018	ExoNet	GPC	RFC	TRICERATOPS	ExoMiner	AstroNet-2023	ExoMiner++
Stellar parameters	†	*	*		*	*	*	†	*	*	*
DV Diagnostic scalars		*	*			*	*		*		*
Other Scalar Values										*	
Unfolded Flux										*	*
Phase-folded Flux	†			*	*	*	†	†	*	*	*
Odd & Even Flux		†	†				†	†	*	*	*
Weak secondary Flux		†	†				†	†	*	*	*
Centroid Motion		†	†		*				*		*
Difference image		†	†				†	†	†		*
Momentum Dump											*
Periodogram											*
Flux Trend											*

inputs from DV reports, including unfolded flux, difference image, and momentum dump data, along with new inputs such as flux periodogram and flux trend data to improve false positive identification. In addition to these expanded inputs, ExoMiner++ features architectural modifications informed by domain expertise, further refining its classification accuracy and interpretability.

3.1. Deep Learning Implementation

After introducing the general architecture of Figure 1, we need to fix the details of the components of this architecture. Similar to our previous ExoMiner model (Valizadegan et al. 2022), we use neural network layers for different components of this architecture. The new architecture, however, has multiple important improvements over the earlier version. Figure 2 shows the new architecture where the major changes from the original one are highlighted using red dotted rectangles. These changes include:

1. We introduced five additional branches to the framework that include: Transit-view Unfolded Flux, Difference Image, Transit-view Folded Momentum Dumps, Periodogram, and Full-orbit-view Folded Flux Trend branches (Figure 2). For each branch, we performed multiple iterations over the design of a minimal stand-alone DNN model (without the use of other branches) in order to design the most suitable branch. Detailed explanations of these branches are provided in Section 4.2.
2. We integrated segments of the convolutional branches from three distinct original branches: Transit-view Folded Flux, Secondary Eclipse Flux, and Odd & Even Flux (middle part of the architecture in Figure 2). All three of these diagnostic tests involve using as input the transit-view of their respective phase-folded flux time series. Furthermore,

in all three cases we are interested in capturing potential transit signatures (or their absence). As the convolutional part of their processing branch functions as a low-level feature extractor, merging them ensures that the same type of low-level features (e.g., existence and shape of the transit) are shared across similar diagnostic tests. Despite this convergence, each diagnostic test retains its individual high-level feature extractor unit. These units remain capable of extracting unique features tailored to the specific requirements of each test.

3. We added a measure of uncertainty in the estimated average value of each bin. This uncertainty is computed during the binning process for each phase-folded time series. This added another channel to the time series inputs. For example, in the original model, the input for the Transit-view Folded Secondary Eclipse Flux branch was 1×31 whereas in the new model it is 2×31 . This uncertainty time series has the same dimensionality as the average binned time series and it is fed to the model as an additional second channel. The dimensionality of these phase-folded and binned time series inputs is shown in Figure 2. We discuss this in more detail in Section 4.2.
4. We removed the transit depth from the Transit-view Folded Flux branch due to the significant difference in transit depth distributions between the two missions, which could lead to challenges in transfer learning caused by distribution shift. However, since self-normalization (Valizadegan et al. 2022) results in the loss of transit depth information, we introduced the minimum value of the Transit-view Folded Flux as a scalar input to this branch to retain crucial depth information and the

- original amplitude of the signal before normalization.
5. We removed the weak secondary depth from the Transit-view Folded Secondary Eclipse Flux branch and replaced it with the minimum value of this time series for the same reason as what was done for the primary transit counterpart. As a result, this branch now includes four scalar values: the minimum value, secondary Multiple Event Statistic (MES), geometric albedo and planet effective temperature comparison statistics (Twicken et al. 2018a; Jenkins 2020).
 6. We removed multiple scalar values from the Transit-view Folded Centroid Motion branch because they are either not accurate or not used for the TESS mission. These are the flux-weighted centroid motion statistics and the difference image centroid offset from the out-of-transit (oot) centroid and its uncertainty. The flux-weighted centroid motion statistic is not computed in the Data Validation (DV) module of the SPOC pipeline for the TESS mission, while the centroid offset from the oot centroid computed from the difference image is not reliable for TESS as it was for Kepler (due to substantial crowding in the photometric apertures of many TESS targets). We instead added the following two new scalar values in this branch: 1) Target star magnitude, *mag*, required to identify saturated stars for which the centroid diagnostic test is invalid, and 2) Renormalized Unit Weight Error (RUWE, Lindgren et al. 2021), which is an indicator of the potential stellar multiplicity of the target. This leads to a total of 4 scalar values for this branch.
 7. We removed the rolling band count statistic (Van Cleve & Caldwell 2016) for level zero from the DV Diagnostic branch since the TESS cameras do not experience rolling band noise. We instead added MES, Max Single Event Statistic (SES), Robust Statistic, and Goodness of Fit Chi Square Statistic (Twicken et al. 2018a; Jenkins 2020; Seader et al. 2013; Seader et al. 2015), all of which are key diagnostics within the transiting planet search (TPS) used to quantify the validity of the putative signal. This led to a total of 9 scalar values for this branch.
 8. We updated the architecture by adding a fully connected (FC) layer at the end of both stellar parameters and DV diagnostic branches to make sure the contribution of each branch is learned

through training instead of being dictated by the architecture. Similar to the other convolutional branches, these FC layers have 4 units each.

9. We use a Savitzky-Golay filter to detrend time series data. In the original ExoMiner model, we used a spline fit to remove low-frequency signals such as stellar variability, following the approach in Shallue & Vanderburg (2018). However, we found that there are many TESS targets with higher frequency signals including sinusoidal stellar variability (Fetherolf et al. 2023a). Such signals can prevent the model from examining the transits hidden in the data. Thus, we replaced the spline filter with the more manageable Savitzky-Golay filter (Savitzky & Golay 1964), based on local least-squares fitting of the data by polynomials, to better remove higher frequency stellar variability.

Some of the minor changes (Items 3-7) in this architecture are reflected in a recent version of ExoMiner used to classify multi-planet systems from Kepler (Valizadegan et al. 2023).

The most important change to the ExoMiner model (Valizadegan et al. 2022) is Item 1 above for which we provide some details below:

- Added Transit-view Unfolded Flux branch: This branch is tasked with processing and extracting information from unfolded flux data. Unfolded flux data are used by SMEs to study the consistency of the transits over different periods. We employed both a Transformer (Vaswani et al. 2023) and a conventional branch for this purpose. After implementing and testing both approaches, we determined that the convolutional branch outperformed the Transformers. Our convolutional branch for unfolded flux data includes a set of convolutional blocks for feature extraction at each phase, an assessment block to evaluate the differences in the extracted features, and a final convolutional layer to extract features on top of the previous assessment block. In the assessment block, we use specific layers to compute the maximum, minimum, and mean values of the features. The details of this branch are depicted in Figure 2. We discuss this in more detail in Section 4.2.
- Added Difference Image branch: In-transit versus out-of-transit difference imaging is essential for detecting offsets in the location of the transit source relative to the target star that may indicate the influence of background objects or nearby stars. A significant difference image centroid offset often suggests that the observed light variation is not due to a genuine planetary transit on the target, but rather to contamination

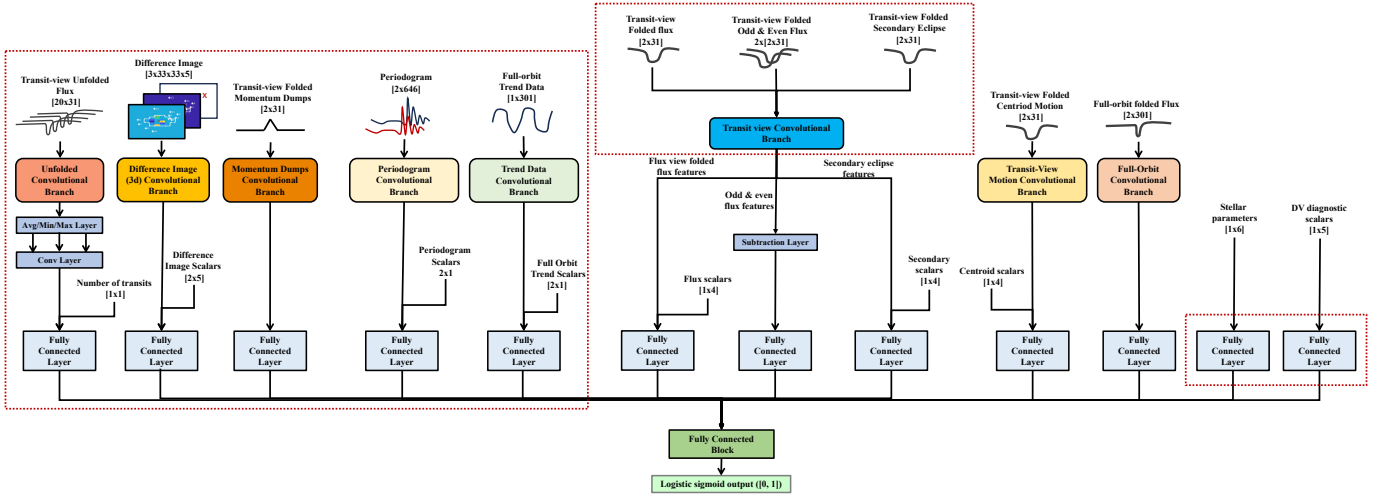


Figure 2. Deep Learning Implementation of the Classification Design in Figure 1.

from other sources. Figure 3 illustrates the usefulness of difference imaging for identifying transits occurring in a nearby star. In this case, the source of TESS SPOC TCE TIC 309787037-1-S35² is not the target star TIC 309787037, but a known nearby fainter star that is located in an adjacent pixel that is included in the photometric aperture. This ability to identify and quantify centroid offsets enhances TESS’s and Kepler’s capacity to filter out FPs, thereby improving the reliability of exoplanet candidate confirmations and providing deeper insights into their characteristics. Thus, we added the Difference Image branch to process difference image data.

- Added Periodogram branch: We included the periodogram of the Pre-search Data Conditioning SAP (PDCSAP) flux (Smith et al. 2012) as a tool to detect and analyze periodic signals in time series data. A periodogram measures the power or variance of the data at different frequencies (or periods), providing insights into power vs. frequency, identification of periodic signals, dominant frequencies, signal strength, and noise harmonics. We included the periodogram to introduce additional data that might not be captured by other diagnostics (e.g., possible information regarding the presence and characteristics of other transits in the system), aiming to enhance performance, particularly in distinguishing brown dwarfs (BD), single-lined spectroscopic binaries (SB1), and double-lined spectroscopic binaries (SB2).

² To refer to a TESS SPOC TCE, we use the naming form of x-y-Sz where x is the target TIC ID, y is the TCE planet number set by the SPOC pipeline, and z is the sector run (if TCE comes from a multi-sector run, then Sz1-z2, where z1 and z2 are the start and end sectors of the sector run, respectively) where it was detected.

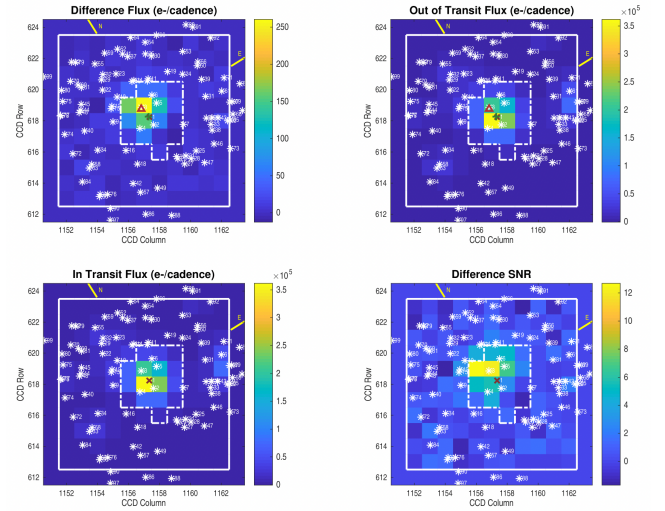


Figure 3. Difference image data for TESS SPOC TCE TIC 309787037-1-S35 (TOI 1046.01, a nearby EB), as shown in the DV mini-report. From left to right, top to bottom, the images show the difference flux, out-of-transit flux, in-transit flux, and difference SNR flux images. The red triangle marks the estimated transit source location, the red cross indicates the TIC’s coordinates in the CCD frame, the green plus represents the out-of-transit centroid estimate, and the white asterisks denote the positions of neighboring stars in the postage stamp. The photometric aperture is outlined with a dashed white line, while the target mask is indicated by a solid white line.

In single-planet systems, exoplanets generally produce cleaner, single periodogram peaks with lower amplitude variations compared to BDs or binaries, which tend to show stronger and more complex signals. Due to their higher-masses, BDs, SB1, and SB2 systems can display multiple periodogram peaks or harmonics, as they induce larger ellipsoidal variations in their par-

ent star, and potentially exhibit Doppler beaming and higher thermal self-emission. However, in multi-planet systems, the presence of additional transits may also lead to a more complex periodogram, with multiple peaks corresponding to the different orbital periods of the planets. In such cases, while the overall signal might be more intricate, the presence of multiple transits can actually indicate that the target transit is more likely to be planetary. This makes the periodogram a useful tool in identifying and analyzing the signals from different types of objects, particularly in more complex systems.

- **Added Full-orbit-view Folded Flux Trend branch:** Given that detrending might remove some informative part of the signal (Stumpe et al. 2012; Twicken et al. 2010; Morris et al. 2020), we build a new branch that receives the Savitzky-Golay fit component as input. The idea is to provide information to the model about components within the flux time series that occur at the time scale of the detected orbital period of the corresponding transit signal, and were fitted during the detrending process. Figure 4 showcases the flux time series for TIC 167526485 in sector 6. We can observe a sinusoidal signal (at half period of the transit event) caused by the ellipsoidal variations that happen in this system due to the gravitational interaction of the binary components. For most exoplanets, these variations will not be in phase with the transit, and so the phase-folded trend will not show such variations. Exceptions to this are massive planets such as hot Jupiters, and also other sources of FPs like BDs. Other potential signals that can show up in the flux trend time series include unmasked transits. Although we mask transits from detected TCEs in the light curve before detrending the time series, uncertainties in ephemerides might lead to the total or partial exclusion of real transits from the detrended time series. Furthermore, unidentified transits are not masked and might be fitted by the detrending model, thus showing up in these data.
- **Added Momentum Dump branch:** This branch is dedicated to processing momentum dump data. Spacecraft reaction wheel momentum management cycles are known to introduce artifacts in the data due to changing pointing behavior. These artifacts can occasionally be identified by the SPOC pipeline as TCEs. Figure 5 highlights the momentum dump events for the flux time series for TIC 82707763 in sector 37. These events are closely aligned with the transits. We implemented a convolutional branch, akin to those used for processing transit view data in the original

ExoMiner model for this particular data input. We discuss this in more detail in Section 4.2.

We will study the effect of each of these new branches in the performance of the model in Section 6.9.

4. DATA PROCESSING

4.1. Data Preparation

In the processing of TESS 2-minute data, the workflow comprised two phases. Initially, data collection spanned Year 1 through 4, encompassing sectors 1–55. This yielded approximately 125,000 SPOC TCEs from 71 transit searches, including 55 single-sector and 16 multi-sector pipeline runs. These data formed the basis for the initial set of experiments for model and experiment development. In the second phase, data from Year 5 sectors 56–67 were incorporated, totaling nearly 208,000 SPOC TCEs across 85 transit searches, with 18 being multi-sector runs.

We leveraged Kepler labeled data to address annotation limitations in TESS data, but still found it necessary to use TESS-specific data for model training and evaluation. Consequently, we sought reliable and credible sources of TESS labels to minimize label noise and potential interference with model training and evaluation. The labels of the TESS 2-minute SPOC TCE dataset were regularly updated using the following procedure:

1. We first obtain reliable labels from the publicly available Exoplanet Follow-up Observing Program (ExoFOP) TESS Object of Interest (TOI) catalog³ in January 2024. This catalog is regularly updated with new TOIs alerted by the TESS Science Office (Guerrero et al. 2021) and then dispositioned by the TESS Follow-up Observing Program Working Group (TFOPWG) based on a variety of observations, including but not limited to TESS data (e.g., radial velocity measurements). The dispositions in this catalog vary in certainty. For instance, planet candidate (PC) and ambiguous planet candidate (APC) TOIs are not confirmed as planets or non-planets, making them unusable for our training and evaluation purposes. In contrast, known planets (KP) — i.e., planets identified outside the TESS mission — and confirmed planets (CP) — i.e., planets identified and confirmed during the TESS mission — offer a high degree of certainty, minimizing label noise in these categories. The CP category also includes BDs. However, to accurately assess our classifier’s performance, we label BDs as

³ <https://exofop.ipac.caltech.edu/tess/>

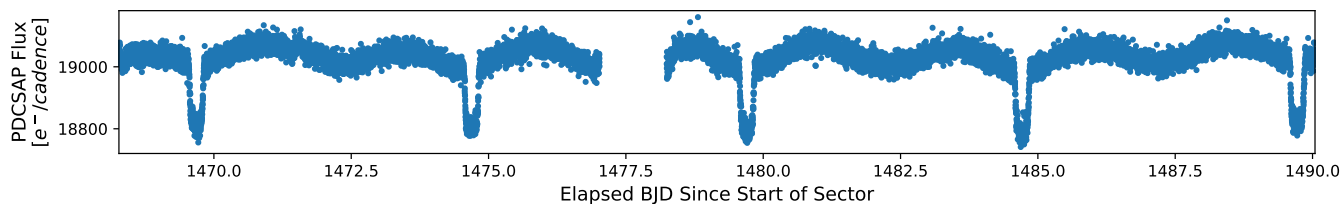


Figure 4. PDCSAP flux for TIC 167526485 in sector 6.



Figure 5. PDCSAP flux for TIC 82707763 in sector 37. The occurrence of momentum dump events is shown as vertical dashed green lines.

non-planets in our dataset, ensuring a more precise evaluation in the presence of BDs.

The FP category in the ExoFOP catalog is based on evidence from both photometric and spectroscopic data. Typically, one of these sources provides conclusive evidence leading to an FP disposition. In summary, we include TCEs labeled as KP, CP, or FP from ExoFOP and exclude those labeled as PC or APC. TCEs without an ExoFOP label are carried forward to the next steps for further labeling.

2. As the next step for the TCEs without any labels (including PC or APC), we use the TESS EB catalog from Villanova⁴ (Prša et al. 2022). This is a catalog of about 4,500 EBs observed during the first two years of the TESS survey. These EBs were manually classified as likely being caused by an on-target EB signal based on light curve shape alone. Thus, the labels are not perfect.
3. For those TCEs without a label in the previous two catalogs, we label them as non-planets if they did not pass the TESS-ExoClass (TEC⁵) flux triage step. These TCEs are deemed non-transiting phenomena (NTP). This catalog was built on the results of TEC up to sector 41.

To utilize labels from the enumerated catalogs above, we performed matching between TESS SPOC TCEs

and the transit signals listed in these catalogs based on their ephemerides (i.e., matching TCEs and transit objects from these catalogs associated with the same TIC ID using their orbital period, epoch of the first detected transit, and transit duration). To achieve this, we followed the same procedure mentioned in (Twicken et al. 2018b). We created a periodic pulse train for each TCE/object based on their ephemerides. These time series span the duration of the sector run under analysis. For each target star in a given sector run, we computed the cosine similarity between each TCE and object for that target star. A TCE was considered matched to an object if its matching score exceeded 0.75 and it had the highest score across all TCEs for that object. This second condition was employed to prevent the matching of objects to secondary transits or residual TCEs. This strict matching procedure minimizes the number of spurious matches, thereby reducing the label noise in our labeled dataset.

Table 2 shows the counts and relative percentage of TCEs in the data set created by our pipeline at the end of the second stage for the TESS 2-min data for six major categories: KP, CP, BD, and FP from ExoFOP, EB from Villanova EB catalog, and NTP from TEC. Those TCEs that could not be labeled were dispositioned as unknown (UNK) and were not used to train nor to evaluate the models. Out of the initial set of 208k TCEs, about 205k were preprocessed successfully. Those that were not preprocessed had been primarily labeled either as NTPs or UNKs.

Multiple TCEs may correspond to the same event due to the multi-sector nature of the TESS mission. For TCEs labeled from the ExoFOP and the Villanova EB catalog, we identify TCEs from the same event using their

⁴ <https://archive.stsci.edu/hlsp/tess-ebc>,
<https://iopscience.iop.org/article/10.3847/1538-4365/ac324a>

⁵ <https://github.com/christopherburke/TESS-ExoClass>

matched TOIs/objects in these catalogs. However, for the NTP category, we do not group TCEs into the same event for two reasons: 1) the non-transiting nature of NTPs means we do not expect to find ephemeris matches in multiple sectors in general, and 2) ephemeris matching for NTPs is computationally expensive due to the lack of reference points, such as a TOI list or the Villanova EB catalog. Table 3 shows the number of events for each category after grouping the TCEs listed in Table 2.

The process of matching TCEs to objects from different catalogs based on their ephemerides is imperfect for several reasons. First, weak secondary events are sometimes detected as separate TCEs, leading to the TCEs corresponding to the weak secondary being left unlabeled (i.e., classified as unknown) despite being known signals. For example, in the case of TIC 16740101, multiple TCEs are detected: some correspond to the primary TESS SPOC TCE TIC 16740101-1- Sz_1 , while others correspond to the weak secondary TESS SPOC TCE TIC 16740101-1- Sz_2 for different sector runs (denoted by different values of z_1 and z_2). While the TCEs for the primary are matched to TOI 1150.01, the weak secondaries remain unmatched to any TOIs and are labeled as UNKs. Although this scenario does not lead to mislabeling, such TCEs should not be classified as UNKs.

Second, the orbital period values can vary across different sectors. In extreme cases, the TCE period and the TOI/object period may differ by factors of 2 or 3. A small error in the period can propagate into substantial mismatches of transit locations over longer sector runs. This issue is further exacerbated by errors in other ephemeris parameters such as duration and epoch, making the matching process even more complex. The following examples illustrate these challenges: 1) TESS SPOC TIC 82308728-1-S14-50: The period is twice that of the planet TOI 1821.01 (KP) because two out of four transits are missing in sectors 22 and 49. This incorrect period results in failed ephemeris matching, leaving the TCE labeled as UNK, 2) TESS SPOC TIC 23434737-1-S1-65: The estimated orbital period of 25.5 days differs slightly from the planet TOI 1203.01 (CP) period of 25.52 days. Although the error is small, it propagates over the data span (sector 1 through sector 65), leading to substantial misalignment, failed matching to the TOI, and an UNK label, 3) TESS SPOC TIC 307210830-2-S35: The transit duration is significantly different from that of the corresponding TOI 175.02 (CP) (about 1.8 times longer than the TOI duration), leading to a failed ephemeris match and UNK label, and 4) TESS SPOC TIC 283722336-1-S17: The transit midpoint location differs significantly from the corresponding planet TOI 1469.01 (KP) due to epoch mismatches. The TCE epoch

originates from sector 17, while the TOI epoch comes from sector 57.

Additionally, data gaps caused by phenomena such as scattered light and momentum dumps further exacerbate these issues. These examples highlight the various scenarios where ephemeris matching can fail, complicating the classification process.

Given that the label we use for TESS comes from different sources that sometimes are not very reliable, we also incorporate Kepler data, which has higher-quality labels, to assist in training our machine learning model. A summary of the Kepler data used in our study is provided in Table 4.

4.2. Preprocessing Pipeline

The preprocessing pipeline was subjected to regular changes as part of the iterative process of data processing and model development. Below, we describe those changes compared to the original model (Valizadegan et al. 2022):

- Momentum Dump pipeline: We extracted information relative to the momentum dumps from the data quality arrays contained in the light curve data for each target (Twicken et al. 2020). We then phase-folded this binary time series using the estimated orbital period for each TCE and binned the signal through mean averaging to the same size as the flux and centroid motion time series. Thus, each bin value reflects the fraction of cadences in the bin affected by the momentum dump according to the respective data quality flag. The location of the peaks in these time series tells us whether the momentum dump events align with the transits of the TCE; the amplitude of the signal tells us the fraction of cadences per bin that were affected by this phenomenon. Figure 6 shows the phase-folded momentum dump flag data using the detected orbital period for TESS SPOC TCE TIC 82707763-1-S37 (top), and its binned version ready to feed to the model for TOI 1991.01.
- Difference Image pipeline: we developed a preprocessing pipeline that first extracts the difference image data from the target DV xml files⁶ for each TCE in the different sector runs, and then preprocesses these data into a format amenable to be fed into our models. This was an involved process requiring several iterations and feedback from SMEs on our team to make the data suitable to be ingested by our models, and

⁶ The format of the archival SPOC products including DV xml file are described in the TESS Science Data Products Description Document at <https://archive.stsci.edu/missions/tess/doc/EXP-TESS-ARC-ICD-TM-0014-Rev-F.pdf>.

Table 2. TESS 2-min TCE Counts. We consider BD, EB, and FP together as one group of Astrophysical FPs or AFPs.

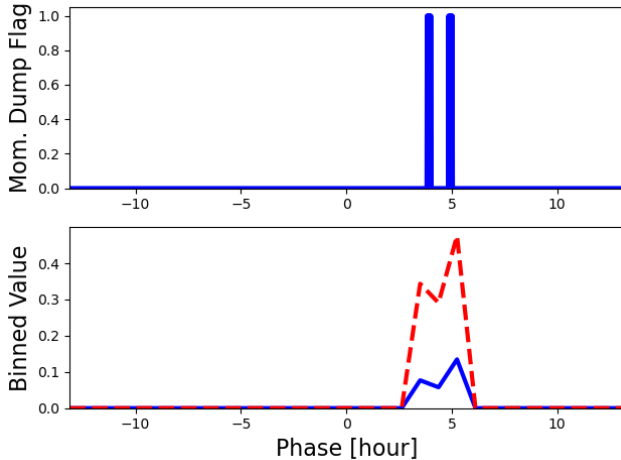
Classes	Exoplanets		Non-planets			
Sub-classes	KP	CP	BD	EB	FP	NTP
Count (Percentage)	1835 (3.21%)	1846 (3.23%)	32 (0.06%)	12738 (22.28%)	1702 (2.98%)	39009 (68.24%)
Total (Percentage)	3681 (6.44%)		53481 (93.56%)			

Table 3. TESS 2-min Event Counts. We consider BD, EB, and FP together as one group of Astrophysical FPs or AFPs.

Classes	Exoplanets		Non-planets			
Sub-classes	KP	CP	BD	EB	FP	NTP
Count (Percentage)	486 (1.13%)	371 (0.88%)	10 (0.02%)	2557 (5.96%)	442 (1.03%)	39009 (90.98%)
Total (Percentage)	857 (2.01%)		42018 (97.99%)			

Table 4. Kepler Counts.

Classes	Exoplanets	Non-planets
Count (Percentage)	2654 (8.58%)	28287 (91.42%)

**Figure 6.** Momentum dump data for TESS SPOC TCE TIC 82707763-1-S37 (TOI 1991.01, classified as a spectroscopic EB). The top panel displays the phase-folded time series for the momentum dump flag array, while the bottom panel presents the corresponding binned version obtained through the preprocessing steps described in Section 4.2. The solid blue and dashed red lines indicate the average binned value and one standard deviation, respectively.

useful in terms of the information and patterns to be used by the models to distinguish false positives due to transit source offsets from the target star. From the difference image data for a single sector, we create the following features:

1. Out-of-transit image: mean image created using all image data for the out-of-transit (oot) cadences. This image is created in the DV module of the SPOC pipeline.

2. Difference image: mean image created by subtracting the in-transit image from the oot image. This image is created in the DV module of the SPOC pipeline.
3. Target position: we map the TIC coordinates of the target to the CCD pixel frame. The target pixel is set to one while all other pixels are set to zero (see detailed description of the preprocessing steps below).
4. Quality metric: this metric is computed in the DV module of the SPOC pipeline and is the correlation between the difference image and the pixel response function (PRF) centered on the centroid of the difference image thresholded at 75% (i.e., correlations $\geq 75\%$ are deemed “good”, while correlations $< 75\%$ are deemed “bad”).

The number of images available per TCE depends on the number of sectors the respective target was observed and the number of clean transits that were observed for the TCE. To make the difference image data input size uniform to the model across examples (i.e., TCEs), we sample with replacement a set of 5 images (i.e., 5 sectors of data in the case of TESS; 5 quarters of data in the case of Kepler). This gives the model the chance to see (when there are multiple sectors of data available) a diverse set of images for a given TCE. Hence, the dimensionality of any image data (i.e., difference, oot, and target images) is $33 \times 33 \times 5 \times 3$, where the first two dimensions are the height and width of the images, the third dimension is the number of sampled sectors/quarters, and the last dimension is the number of images, one for out-of-transit image, another for difference image, and the last for the target position. For the quality metric the dimensionality is then 1×5 , since this feature is a scalar value for each sector of sampled difference image data.

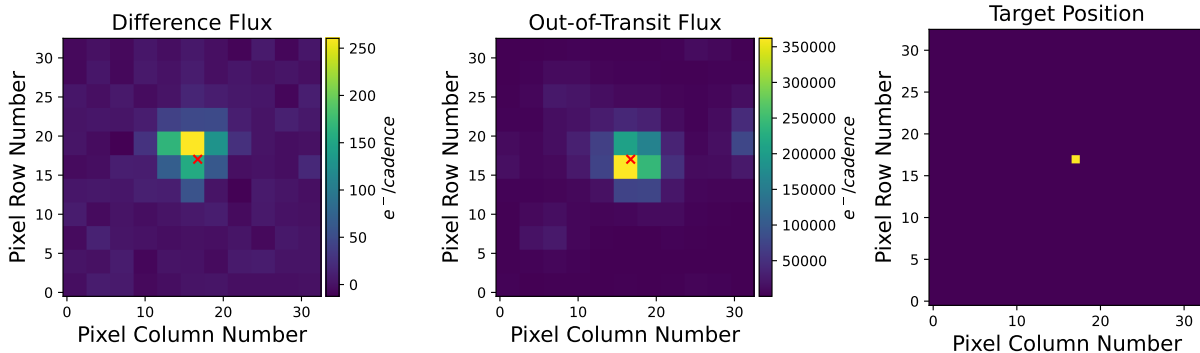


Figure 7. Preprocessed difference image data for TESS SPOC TCE TIC 82707763-1-S37 (TOI 1046.01, a nearby EB), following the steps outlined in Section 4.2 without normalization. From left to right, the panels display the difference image, out-of-transit image, and target position image. In the difference and out-of-transit images, the red cross marks the location of the target, TIC 309787037, with its coordinates mapped to the CCD frame. In the target position image, the pixel containing the target is highlighted in yellow.

On average, Kepler and TESS targets have postage stamps with dimensions 5×6 px and 11×11 px, respectively. Brighter targets and cases in which the target is close to the edge of the CCD lead to changes in the size and shape of the aperture, thus leading to out-of-transit and in-transit images with different sizes. Since the model requires uniform dimensions across all examples, we need to go through a preprocessing step to make all images the same size. Given that the majority of TESS targets have 11×11 px, we transform all images to that size, thus minimizing the amount of transformation performed to the images for TESS targets, and ensuring that the majority of Kepler targets’ images are filled to that size without resorting to any image cropping. Furthermore, less than 20% of the TESS TCEs in our dataset come from targets whose images are larger than 11×11 px, and this subset of cases comes mostly from bright stars that are more likely to saturate the image data. In such scenario, it is less likely that the images contain useful information for estimating the transit source offset.

After sampling the set of images for a given TCE, we execute multiple steps to address missing values and size differences. We set negative out-of-transit pixels to missing in both out-of-transit and difference images, and fill out missing values using nearest neighbors with a 3×3 px window with the same weights for all non-missing pixels. If the images are smaller than 11×11 px, we pad them by extending the edges. Given that the target location is provided at the subpixel level, we resize the images through nearest neighbor interpolation using a factor of 3 so all images are at least 33×33 px after this step. By doing this, each pixel becomes a 3×3 grid that we can use to more accurately describe

the subpixel location of the target. Finally, for images that are larger than the desired final size, we crop them relative to the center pixel so they become 33×33 px. The image data is standardized using the median and standard deviation statistics computed across all pixels and images from the training set examples. Figure 7 shows the three input channels of different image data for TESS SPOC TCE TIC 309787037-1-S35 that are fed to the difference image branch after normalization. The difference image suggests that the transit signal does not originate in the target star (TIC 309787037 with $T_{mag} = 10.012$), but from a neighboring star, observed in a different pixel. A known nearby, fainter star, TIC 309787035 ($T_{mag} = 16.480$), is located at this location.

- **Unfolded Flux pipeline:** The number of observed phases for a detected TCE is a function of the observation time for the respective target, the orbital period of the TCE, and the number and size of gaps in the data during that observation. For this reason, the number of transits across TCEs can vary significantly. To make these data uniform across TCEs, so that it can be amenable to be ingested by our models, we sample with replacement a set of 20 transit signatures, with each binned to a fixed size (more concretely, 31 bins for the transit view). These phases are normalized using the same median and minimum statistics computed from the corresponding phase folded and binned transit view time series. To give the model information about the number of valid transits that are observed in the data, we add as a scalar input feature to this branch the number of transits observed by the SPOC DV pipeline for any given TCE. For completeness, we also add the number of transits expected by the SPOC DV pipeline, which could provide some

information about missing data. Figure 8 shows the non-normalized unfolded flux data that are fed to the unfolded branch of ExoMiner++ after normalization.

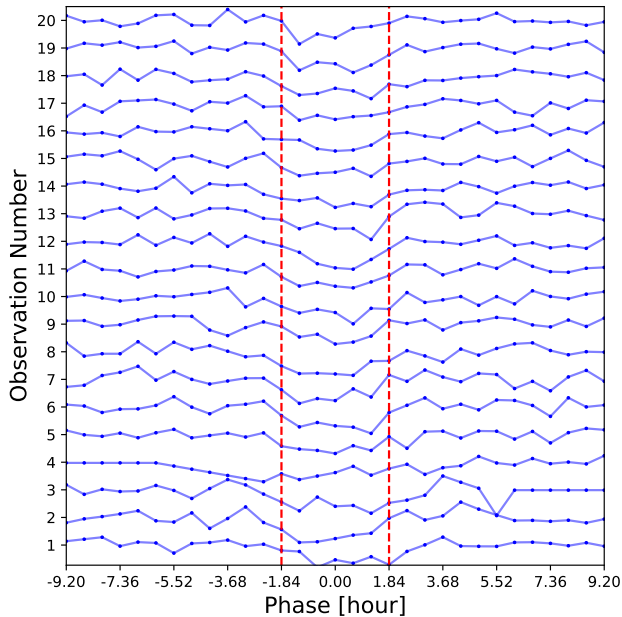


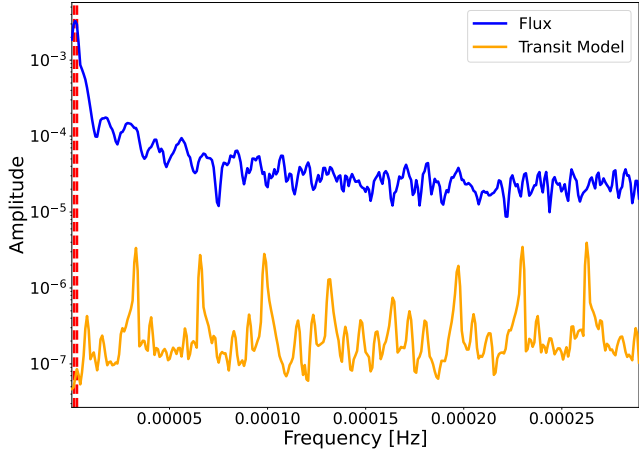
Figure 8. Unfolded binned flux data for TESS SPOC TCE TIC 98545929-1-S1-36 (TOI 1916.01, KP). The red dashed lines highlight the transit duration estimate of the detected TCE (~ 3.68 hours) centered on the estimated transit midpoint.

- **Periodogram pipeline:** We applied the Lomb-Scargle periodogram (Lomb 1976; Scargle 1982) to estimate the spectral density of the flux time series prior to detrending. This approach allows the periodogram to capture additional signals present in the time series, such as stellar variability, which are typically removed during the detrending process. The periodograms are computed for a period range that spans 0.04 days to 54 days. This allows us to capture information for even the shortest period TCEs (~ 0.2 days; so the range extends to at least 5 harmonics for any TCE) and covers approximately two sectors of observation. About 11.5% TCEs in our dataset show a period longer than 54 days⁷. Out of those, we count only 12 unique planets and 7 unique EBs. We chose this observation time as a trade off between periodogram feature complexity and the number of long-period TCEs whose transit periodicity falls outside of the range set for the periodogram. Nevertheless, even for those scenarios

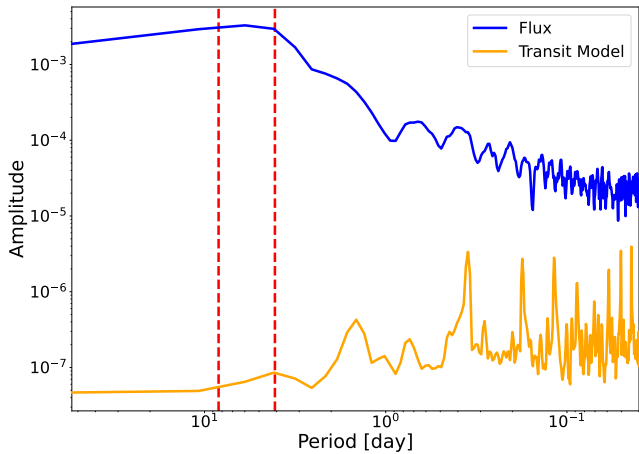
⁷ For many of these the true period is ambiguous and may be (significantly) shorter.

the periodogram can reveal information about other signals in the light curve data. The frequency values are defined linearly across the range using a downsampling factor of 4 to reduce the dimensionality of the feature array. The periodogram is normalized to show the amplitude values, and then smoothed to remove noise using a box kernel filter of width 2. Finally, the periodogram is normalized by its maximum amplitude so all examples fed to the model are defined in $[0, 1]$ interval. Information about the maximum power is conveyed to the model as a scalar feature. This feature is standardized using training set statistics following the same methodology applied to all other scalar features. To provide to the model information about the location and characteristics of the TCE signal in the frequency domain, we create another periodogram using the same methodology described for the one created from the flux data. Using the estimated period, transit duration, secondary offset, and transit depths of the primary and secondary events, a simple transit model is created by setting primary and secondary in-transit cadences to the corresponding transit depth, with out-of-transit cadences set to the median value of the original flux time series. By design, the periodogram of this time series will show peaks for the period and harmonics of the detected TCE, thus revealing to the model where in the frequency domain there is relevant information related to the TCE transit signal. The model can use that information to compare the features in the periodogram of the data to a periodogram specific to the transit model associated with the TCE. Figure 9 shows an example of the periodogram data that are normalized and then fed to the model.

- **Detrending pipeline:** we changed the detrending method from employing a spline in the original ExoMiner to using a Savitzky-Golay filter to remove low-frequency trends in the data. We used a window length of 1.2 days, and chose the best fitting model (up to maximum 8th degree polynomial order) using Bayesian information criterion (BIC; Schwarz 1978; Stoica & Selen 2004) with a penalty weight of 1 for model selection. We masked the in-transit cadences of all detected transits in the light curve before fitting any model, and the raw time series was split into smaller segments if the gap between two consecutive samples was larger than 5 times the nominal cadence duration. A sigma value of 5 was used to remove outliers from the detrended flux time series. A similar approach was used to detrend the centroid motion time series. Figure 10 shows an example of flux trend data before it is normalized and fed to the model. In this case,



(a) Frequency scale.



(b) Period scale.

Figure 9. Periodogram data for TESS SPOC TCE TIC 232568235-1-S24 (TOI 2260.01, CP) after preprocessing, as described in Section 4.2, without normalization. The figures display the flux and transit model periodograms. TOI 2260.01 is classified as a CP orbiting a variable star. The red dashed lines indicate the estimated periods of a double-sinusoidal function fitted to the photometric variability of TIC 232568235, derived from Fetherolf et al. (2023b).

the ellipsoidal variations occurring at half period of the EB in TIC 167526485 are made even more clear by phase-folding the flux trend time series using the orbital period of the corresponding TCE.

- Uncertainty for the phase-folded and binned time series: for each bin in the phase-folded time series, the standard deviation of the values is computed along with the median value. The standard error of the mean is then computed by normalizing the standard deviation by the square root of the number of points within the bin to provide information to the model regarding the uncertainty in the average estimation.

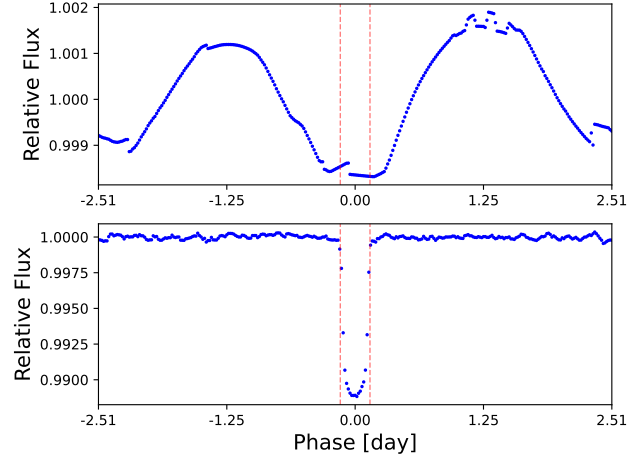


Figure 10. The top and bottom figures show the phase-folded, binned trend and detrended flux time series for TESS SPOC TCE TIC 167526485-1-S6 (dispositioned as an EB in Prša et al. (2022)), respectively, without normalization. The red dashed lines indicate the estimated transit duration for this TCE, centered around the estimated transit midpoint.

5. HYPERPARAMETER OPTIMIZATION AND MODEL TRAINING

Early in our work, we conducted a hyperparameter optimization (HPO) study with initial data from the TESS Mission. The goal was to find a configuration of *ExoMiner++* that would be optimized for TESS data, as opposed to the previous *ExoMiner* developed for Kepler. Using a Bayesian/Hyperband method (Falkner et al. 2018), we evaluated a total number of 177 configurations over the course of 3 days and using a V100 GPU node from the NASA Advanced Supercomputing Facility. For each configuration evaluated, an average score ensemble of three models was trained on the provided budget, and the precision-recall area under curve (PR AUC) on the validation set for this ensemble was set as the optimization metric for the HPO framework (i.e., a configuration with a higher PR AUC on the validation set is “better”).

The set of hyperparameters from the best configuration found in this HPO run was used in the *ExoMiner++* for the experiments described in Section 6. Appendix A describes the details of the architecture and optimization parameters.

To evaluate the performance of our optimized *ExoMiner++* model, we used 10-fold cross-validation, following the approach in Valizadegan et al. (2022). The target stars were divided into 10 equal subsets, with the TCEs from one subset serving as the test set while the remaining 9 subsets were used as the training and validation sets (1 subset was reserved for validation). This

process was repeated for all folds, ensuring that each subset was used once as the test set.

The motivation behind cross-validation is to ensure that the model performs well not only on the data seen during training but also on unseen data, thereby simulating real-world conditions. By dividing the data into multiple subsets and iteratively testing on each subset, the model’s performance is evaluated on every part of the dataset. This approach reduces the risk of overfitting, where the model performs well on training data but fails on new data. Cross-validation provides a robust measure of the model’s ability to generalize to new target stars, making it a critical step in assessing its overall reliability (Hastie et al. 2009).

For each cross-validation iteration, a set of 10 models was trained, and an ensemble model was created by averaging the scores of the 10 models. This procedure minimizes the effects of stochasticity in the training process. By training multiple models with different weight initializations, the ensemble captures variations in local minima encountered during the optimization of the loss function, resulting in a more robust representation of the model’s behavior and performance.

All models were trained for 300 epochs, optimized using binary cross-entropy as the loss function and the Adam optimizer (Kingma 2014) ($\beta_1 = 0.900$, $\beta_2 = 0.999$, $\epsilon = 1e-8$). Early stopping with a patience of 20 epochs was employed to prevent overfitting. If no improvement in the validation PR AUC was observed after 20 epochs, the training was stopped, and the model instance at that point was selected as the final model.

Table 5 provides a detailed list of all TCEs in our dataset, including their ephemeris information and the scores obtained from all models evaluated in this study using 10-fold cross-validation.

6. PERFORMANCE STUDY

6.1. Evaluation Metrics

ExoMiner++ not only assigns a binary label to each TCE — 1 for planets and 0 for non-planets — but also provides a confidence score between 0 and 1 associated with the label. This score reflects the model’s certainty about its classification, with values closer to 1 indicating a higher confidence in the planetary nature of the TCE, and values closer to 0 signaling stronger confidence in the non-planet classification. These scores are particularly useful for ranking and prioritizing TCEs for further human inspection and for identifying cases that may require additional scrutiny due to intermediate confidence levels. By combining both labels and confidence scores, ExoMiner++ provides a comprehensive framework for au-

Table 5. Scores of different classification model used in this work on the TCEs that are assumed labeled (Table 2) The model label can be obtained by score > 0.5 . This table describes the available columns. The full table is available online.

Column	Description
uid	unique id that includes TCE TIC ID and sector run
target_id	TCE TIC ID
tce_plnt_num	TCE planet number
TOI	TOI number
fold	a value between 0 and 9 indicating the cross-validation fold for that TCE
tce_period	SPOC TCE period
tce_duration	SPOC TCE duration
tce_prad	SPOC TCE planet radius (Earth Radii)
MES	SPOC TCE MES
original_label	KP, CP, BD, EB, FP, or NTP
binary_label	1 for KP and CP, 0 for BD, EB, FP, or NTP
tess-individual	Score by the model trained on TESS
tess-aggregate	Score by the model trained on TESS but aggregated using strategy in Section 6.3
tess+kepler-individual	Score by the model trained on TESS+Kepler (Transfer learning idea in Section 6.2)
tess+kepler-aggregate	Score by the model trained on TESS+Kepler but aggregated using strategy in Section 6.3
DV full report	The URL to the DV full report in the MAST
DV summary report	The URL to the DV summary report in the MAST
DV mini report	The URL to the DV mini report in the MAST

tomating transit classification while enabling nuanced analysis of the results.

To measure the overall performance of the model on the binary classification problem of exoplanet versus non-exoplanet, we use the following metrics:

- **Accuracy:** Accuracy measures the proportion of correctly classified instances out of the total instances. It is defined as:

$$\text{Accuracy} = \frac{\text{True Positives} + \text{True Negatives}}{\text{Total Population}}$$

It is useful when the classes are balanced but can be misleading if the dataset is imbalanced.

- **Precision:** Precision quantifies how many of the instances classified as positive are actually positive. It focuses on the relevance of the positive predictions and is calculated as:

$$\text{Precision} = \frac{\text{True Positives}}{\text{True Positives} + \text{False Positives}}$$

Precision is important when the cost of false positives is high.

- **Recall** (Sensitivity or True Positive Rate): Recall measures how many actual positive instances were correctly identified. It focuses on detecting all positive instances and is given by:

$$\text{Recall} = \frac{\text{True Positives}}{\text{True Positives} + \text{False Negatives}}$$

Recall is critical when missing positive instances has a high cost.

- **PR-AUC** (Precision-Recall Area Under Curve): PR-AUC is the area under the Precision-Recall curve, which plots precision against recall at different thresholds. It is a better metric than accuracy for imbalanced datasets where the positive class is rare because it focuses on the performance on the minority class.
- **ROC-AUC** (Receiver Operating Characteristic Area Under Curve): ROC-AUC is the area under the ROC curve, which plots the True Positive Rate (recall) against the False Positive Rate at different thresholds. A higher AUC indicates a better-performing model. It is widely used for binary classification problems and is effective for evaluating models across different decision thresholds.

Besides classification, we are also interested in the quality of the scores generated by `ExoMiner++` for ranking TCEs. High-quality scores imply a more effective catalog that can help prioritize exoplanet candidates. A classifier that ranks exoplanets higher than false positives is preferred, as it enables more efficient follow-up efforts. To assess the model’s ranking performance, we use `Precision@k` or `P@k`:

- **Precision@k or P@k**: `P@k` measures the fraction of relevant instances (exoplanets) among the top k predictions:

$$\text{P@k} = \frac{\text{Number of relevant items in the top } k \text{ results}}{k}$$

where k is a predefined number of top results to evaluate.

These classification and ranking metrics together provide a comprehensive view of the model’s performance from multiple perspectives, depending on the specific needs of the problem (e.g., handling imbalanced classes or managing the cost of false positives and false negatives). Additionally, we report the model’s performance across various sub-classes — e.g., KP, CP, EB, BD, FP, and NTP — using recall, which reflects the percentage of each sub-class correctly classified.

6.2. Transfer Learning

Due to the lack of gold-standard labels for TESS, we leveraged Kepler data to enhance performance. Initially, we experimented with various transfer learning approaches (Ng 2016), such as training on Kepler data and fine-tuning certain layers of the model using TESS data. However, as TESS data grew in size and label quality, a simpler approach of combining Kepler and TESS data to create a larger training set proved more effective. In this approach, we incorporated Kepler data into the training set of all cross validation iterations, ensuring that the validation and testing were performed only on TESS data.

6.3. Multi-Sector Aggregation of the results

Given the multi-sector nature of the TESS mission and the fact that many target stars are observed across multiple sectors, the same event is often detected as different TCEs in both single-sector and multi-sector runs. With more data for an event, we achieve a higher SNR and a more reliable signal for those TCEs. Naturally, the longest sector runs (i.e., the TCEs with the largest number of transits observed) provide better data for classifying that event. One could argue that only the longest sector runs should also be used to train the classifier. However, since a significant portion of target stars are not observed in multiple sectors, and the classifier must perform well on those too, we include all TCEs detected by the pipeline in the training. Including shorter-run TCEs (even for events with longer sector runs) exposes the classifier to more low-SNR signals, ensuring it performs well across all targets and generalizes better to low-SNR cases. This results in classifying the same event multiple times—once for each TCE associated with that event. To consolidate this, we generate a single model score/label in post-processing for all TCEs of the same event based on the result of the model for the longest sector run, which ultimately improves overall performance, as we see in Section 6.4.

6.4. Classification performance

Table 6 presents the performance results of `ExoMiner++` on TESS data across various models and strategies, using standard binary classification metrics. Each row corresponds to a different training set (either TESS only or TESS+Kepler for transfer learning) and indicates whether score aggregation was applied after obtaining predictions from `ExoMiner++`. For comparison, we also report the baseline results of `ExoMiner++` when trained and tested on Kepler data.

First, note that the transfer learning and multi-sector aggregation methods, introduced in Sections 6.2 and 6.3, improve overall performance across all binary class metrics; overall, the model trained on the combined Kepler

Table 6. Results of *ExoMiner++* on labeled TESS data set. The best performer is highlighted by bold.

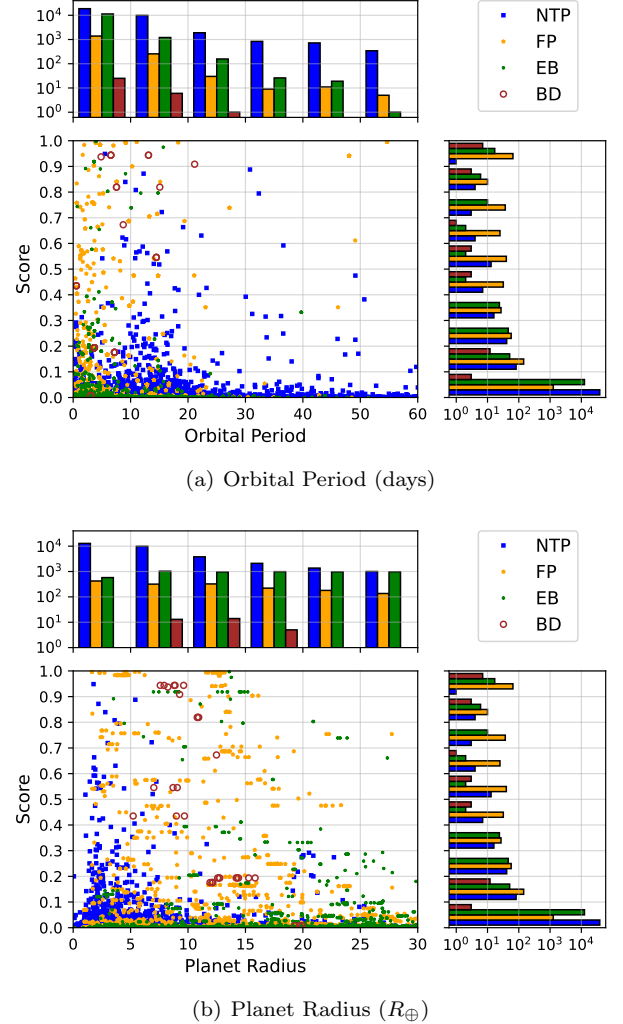
Training	Test	Strategy	Binary results				Recall for subclasses					
							Exoplanets		Non-planets			
Training	Test	Strategy	Precision & Recall	PR AUC	ROC AUC	Accuracy	KP	CP	BD	EB	FP	NTP
TESS	TESS	Individual	0.918 & 0.917	0.966	0.995	0.989	0.939	0.894	0.531	0.995	0.886	0.999
		Aggregate	0.926 & 0.945	0.967	0.995	0.992	0.953	0.938	0.469	0.996	0.890	0.999
TESS+Kepler	TESS	Individual	0.924 & 0.927	0.970	0.997	0.990	0.945	0.909	0.719	0.996	0.887	0.999
		Aggregate	0.933 & 0.951	0.976	0.998	0.992	0.957	0.944	0.562	0.997	0.896	0.999
Kepler	Kepler	N/A	0.976 & 0.965	0.994	0.999	0.995	N/A					

+ TESS data using the multi-sector aggregation strategy achieved the best results.

Second, both transfer learning and multi-sector aggregation strategies enhance performance across nearly all sub-classes. However, for BD, these strategies have a negative effect. Two possible reasons explain this: 1) only 10 BDs are observed accounting for 32 TCEs, and the small number of instances increases uncertainty in the results, and 2) photometric data for BDs is generally indistinguishable from exoplanets, so a more accurate model relying solely on photometric data may perform worse on the BD sub-class.

To further investigate the regions in parameter space where *ExoMiner++* tends to misclassify different non-exoplanet sub-classes, we present in Figure 11 a scatter plot of scores versus orbital period and planet radius. An idea model gives a small score to all the instances of these sub-categories. Our model does a reasonable job on EB and NTP sub-classes. For BDs, *ExoMiner++* performs well when $R_p > 10R_\oplus$, likely due to the larger size of these objects, which aids classification. Additionally, the score distribution for the FP sub-class spans the entire range from 0 to 1, highlighting the inherent difficulty of correctly classifying FPs for *ExoMiner++*. However, no clear pattern emerges regarding the model’s difficulty within specific regions of planet radius and orbital period parameter space.

Table 6 summarizes the precision and recall values at a fixed cutoff threshold of 0.5 for the classifier’s output. To visualize the trade-off between precision and recall across different cutoff thresholds, the PR curve is shown in Figure 12(a). As evident from the curve, aggregate models consistently outperform individual models across a range of threshold values. Furthermore, transfer learning significantly improves performance across thresholds. Figure 12(b) illustrates the score distributions for various models. A model that places the majority of instances near the extremes (close to zero or one) demonstrates higher confidence in its predictions. *ExoMiner++* exhibits the highest confidence on Kepler data, with both transfer

**Figure 11.** Score distribution versus orbital period (left) and planet radius (right) of non-exoplanets categories for TESS+Kepler-Aggregate model.

learning and aggregation strategies further enhancing *ExoMiner++*’s confidence in its classifications.

The previously reported results indicate that *ExoMiner++* performs significantly better on Kepler data compared to TESS. A possible explanation for this disparity might be TESS’s shorter observation windows,

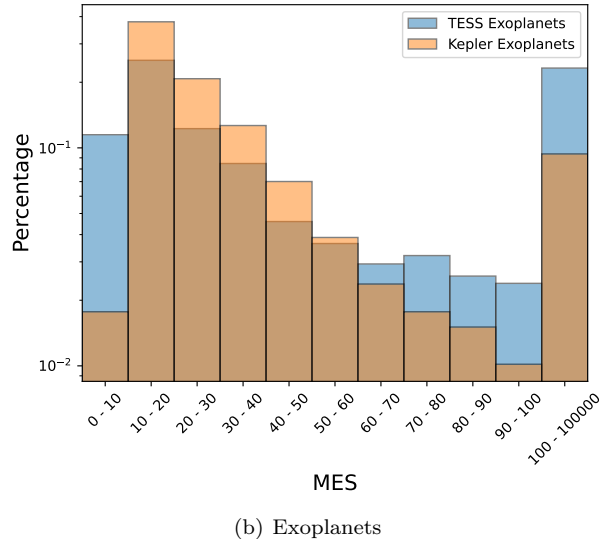
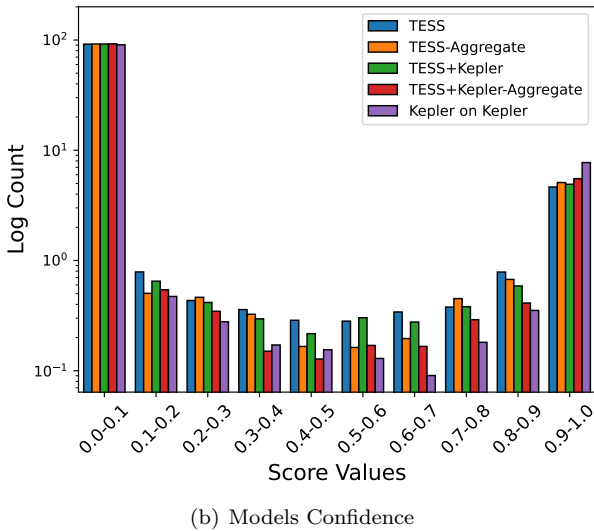
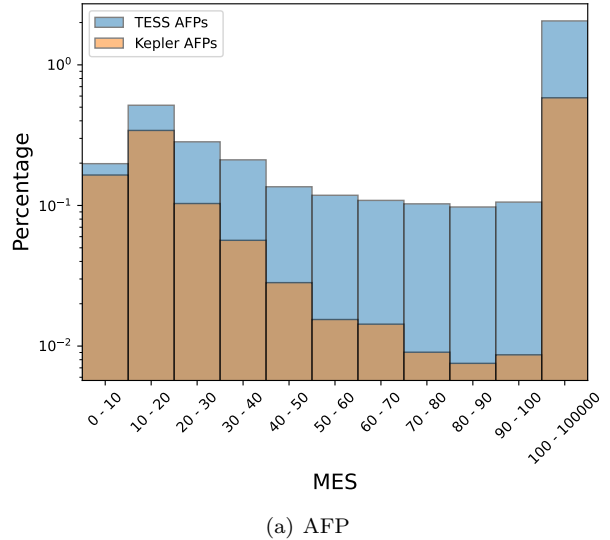
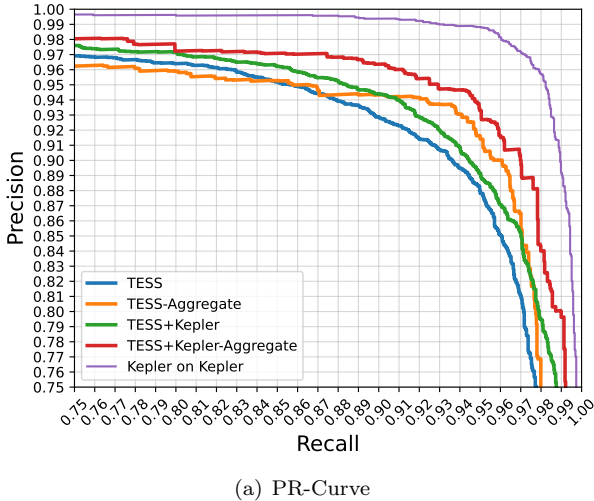


Figure 12. PR-Curve and Confidence of different models.

which could result in lower signal-to-noise ratios (SNR) for TCEs. To investigate this, we plotted the MES value distributions for Kepler and TESS. MES, or Multiple Event Statistic, is a measure used in transit photometry to quantify the statistical significance of a transit signal detected in the light curve of a star. It represents the SNR of a candidate transit event, aggregated over multiple transit events. The MES is calculated by summing the squared SNRs of individual transits, weighted by their uncertainties, and taking the square root. Figure 13 shows the MES values for both exoplanet and AFP populations in TESS SPOC TCEs (i.e., EBs, FPs, and BDs). Notably, there are more exoplanets with $MES < 10$ in TESS than in Kepler, primarily due to two factors: 1) most Kepler exoplanets were validated using a $MES > 10$ or $MES > 10.5$ threshold, and 2) some exoplanets in TESS’s KP category, previously detected

Figure 13. Kepler versus TESS histograms of MES with a focus on values > 10 for exoplanets (KP+CP) and AFPs (EB+FP+BD).

by other telescopes, exhibit lower MES values in TESS data due to its relatively small aperture (10 cm) and shorter observation periods.

Beyond this, Kepler shows a greater number of TCEs in the lower MES bins, while TESS dominates the higher MES bins in Figure 13. Still, Kepler was able to produce more TCEs with very high MES values. To illustrate this, Figure 14 presents a histogram of exceptionally high MES values, showing that Kepler yields significantly more TCEs with very high MES scores. However, MES values > 10.5 are generally considered high enough for reliable planetary candidate identification. Thus, one might say the main reason for the inferior performance of

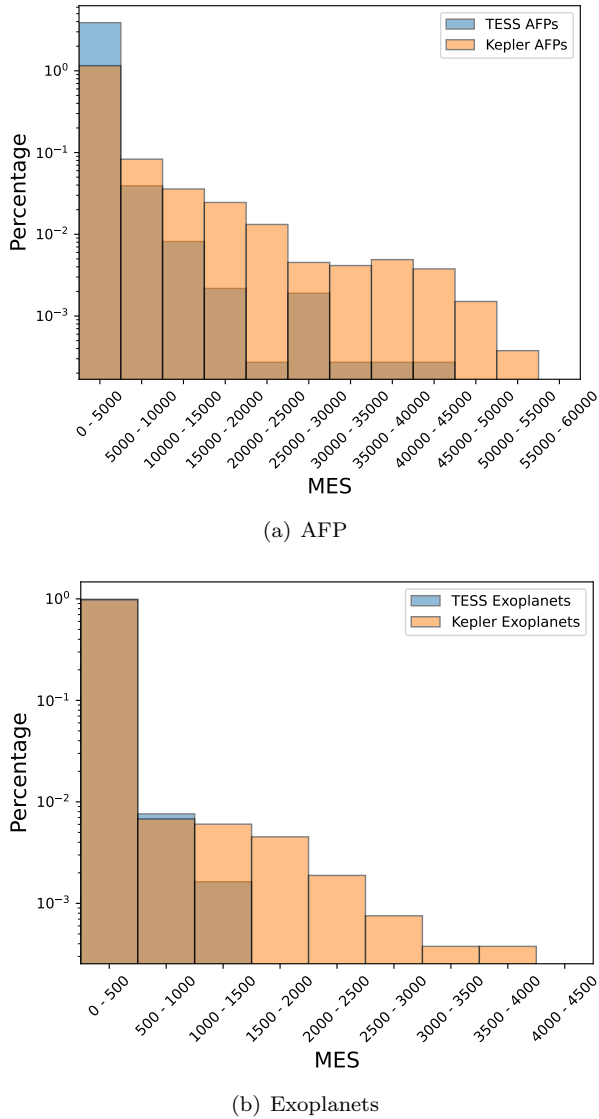


Figure 14. Kepler versus TESS histograms of large values of MES for exoplanets (KP+CP) and AFPs (EB+FP+BD).

the model on TESS compared to Kepler is the existence of numerous exoplanets with low MES values in TESS.

To examine this hypothesis, we plotted in Figure 15 the precision and recall values of different part of the MES versus orbital period and planet radius parameter space for the TESS+Kepler-Aggregate model. Even though the performance of the model on some planet radius bins for small MES values ($MES < 10.5$) is lower compared to larger MES values, the number of misclassified TCEs in those bins is a very small percentage of the total misclassified instances. To confirm this, we removed the exoplanet TCEs with $MES < 10.5$ from the data set and remeasured the model performance. This resulted in the lower values of precision and recall.

Therefore, the question remains: Why does the model perform better for Kepler than for TESS? Section 6.7 explores this key question, with implications for model trust and validation.

6.5. Ranking Performance

Figure 16 shows Precision@ k for various k values and models. Given that our dataset contains 3681 exoplanet TCEs, we plot Precision@ k up to $k = 3600$. The models perform well in ranking exoplanets near the top. Notably, the top 600 ranked by TESS+Kepler-Aggregate model and top 200 TCEs ranked by all models are exoplanets. At $k = 1000$, all models achieve a Precision of at least 0.99, meaning 990 out of the top 1000 TCEs are exoplanets. By $k = 3000$, Precision remains 0.977 for the TESS+Kepler-Aggregate model, indicating that only around 70 out of the top 3000 are not exoplanets. These indicate that **ExoMiner++** is highly reliable for follow-up study or validation to find new exoplanets.

It is also important to emphasize that, in our dataset, the label quality of the positive class (exoplanets) is much higher than that of FPs. This suggests that the Precision@ k for different k values is likely even better than what is reported here. Overall, this demonstrates that our models are highly effective in selecting the most likely exoplanet candidates for follow-up studies or validation.

To further examine the distribution of misclassified instances among the top k TCEs, we plot in Figure 17 the count of misclassified TCEs within each category (NTPs, BDs, EBs, and FPs) from Table 3. The majority of top-ranked misclassified cases belong to the FP class, followed by a smaller number from EBs, with even fewer from the NTP and BD categories. This trend aligns with Table 6, which shows the FP class as the most challenging and the NTP subclass as the least. Despite the limited number of BDs in the dataset, it is notable that the first BD TCE appears at position 2800 for the TESS+Kepler-Aggregate model, indicating that **ExoMiner++** effectively assigns lower scores to BDs compared to exoplanets, even though some BDs are still misclassified (score > 0.5). We will discuss this further in Section 6.7.

6.6. ExoFOP's FP Subcategories Performance

The ExoFOP disposition is derived from two initial dispositions: photometric and spectroscopic. The mapping from these two dispositions to the final ExoFOP disposition depends on the evidence present in the available datasets. For example, if strong evidence of a false positive is found in the photometric data (such as a confirmed nearby EB), the ExoFOP disposition will be classified as FP. Similarly, if there is strong evidence of a stellar companion orbiting the target star at the TESS

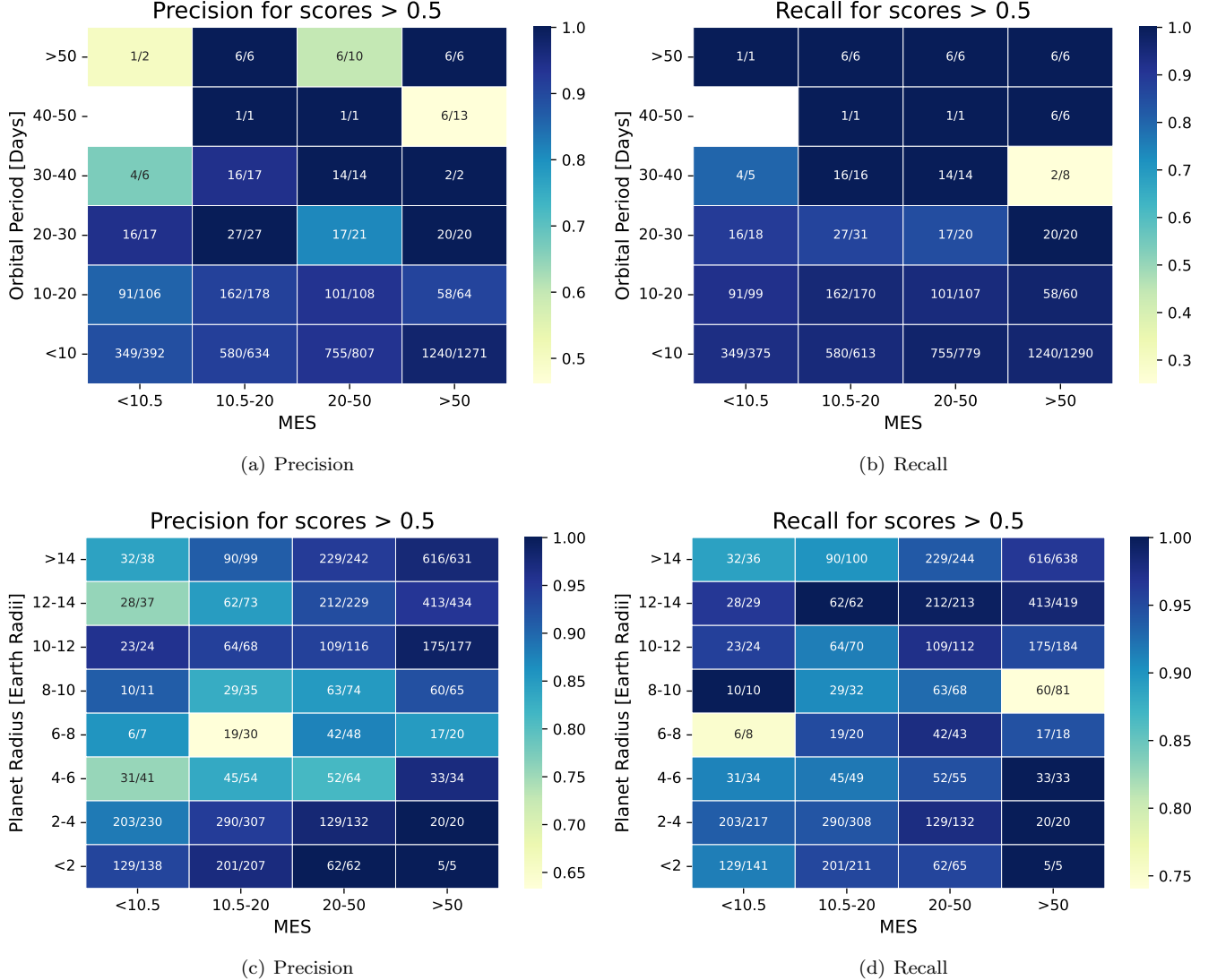


Figure 15. Precision and recall heatmaps as functions of MES, orbital period (days), and planet radius (Earth radii). White cells indicate regions with insufficient data, where the denominator is zero.

ephemeris, then the master disposition will take on the spectroscopic SEB1 disposition, which is then converted to FP on ExoFOP. Typically, one of the photometric or spectroscopic evidences is clearly more conclusive. In Sections 6.6.1 and 6.6.2 below, we provide a performance study of ExoMiner++ on the subcategories for both the photometric and spectroscopic dispositions.

6.6.1. Photometric Disposition

The photometric disposition includes 20 distinct label assignments, ranging from KP and CP to EB and false alarms (FAs), each with varying degrees of label certainty. These subcategories are subsequently mapped to a final ExoFOP disposition using all available information. Some subcategories, such as VPC+ or PC, initially lean toward the exoplanet classification but are later

reclassified as part of the FP category in the final ExoFOP disposition following additional follow-up studies, including spectroscopic observations. Since performance metrics for KP and CP have already been reported in Section 6, we now shift our focus to the photometric subcategories mapped to ExoFOP’s FP category, the only other ExoFOP category included in our dataset. To ensure a meaningful performance assessment, we limit our analysis to FP subcategories with at least 30 instances.

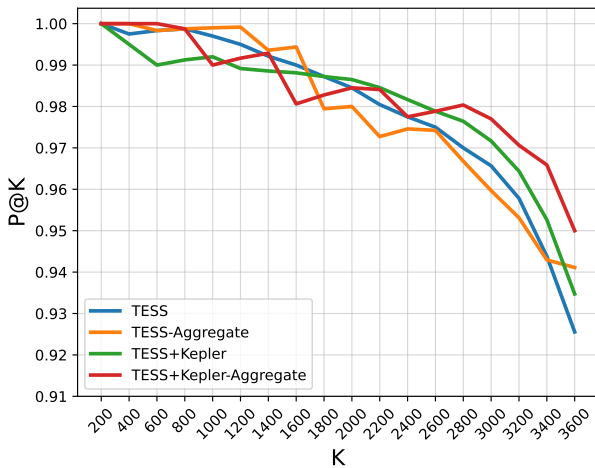
Table 7 lists the photometric disposition labels with more than 30 instances and their counts, and Table 8 shows the model performance for each category. We would like to emphasize that the counts we see in Table 7 only correspond to the FP category in Table 2. This is because the only subcategories in photometric disposition

Table 7. Labels description of ExoFOP’s photometric disposition for FP ExoFOP disposition. Only labels with more than 30 TCEs assignment are shown.

	nmb	Name	Shortened Description	Count
1	VPC+	Verified Achromatic PC	The event has been verified by SG1 to occur within the target star’s follow-up aperture, with no strong filter-dependent depth chromaticity or contamination from nearby Gaia DR2 or TIC stars bright enough to explain the TESS detection. Such planet candidates are usually retired from SG1 but may remain active for light curve collection in other filters.	88
2	VPC-	Verified PC, but follow-up aperture is contaminated	The event has been confirmed within the target star’s follow-up aperture, but there are other stars from Gaia DR2 or TIC that are bright enough to potentially contaminate the TESS detection.	42
3	VPC	Verified PC	SG1 verified within target aperture; no bright Gaia DR2 contaminants.	179
4	PC	PC	Planet candidate with no or inconclusive follow-up observations.	257
5	NEB	Nearby EB	Nearby EB contamination confirmed by follow-up photometry, usually over two epochs. NEB disposition can be assigned directly if TESS centroid data strongly supports the initial detection.	808
6	NPC	Nearby PC	The TESS detection is from an event on a nearby star, which might have a potential planet. The star will get a new TOI number with a PC disposition, and the NPC TOI will be retired as a false positive.	92
7	BEB	Blended EB	The TESS detection likely results from an EB blending. It is classified as BEB due to chromatic depth, lack of RV variation, or correlated bisector span. If followed by ‘?’ (i.e., BEB?), it’s tentative and needs more observations.	42
8	EB	Eclipsing Binary	The TESS detection likely comes from an event at the target star that is too deep for a transiting planet. It may show odd-even depth differences, eccentric EB traits, or indicate a giant star with a stellar companion.	126

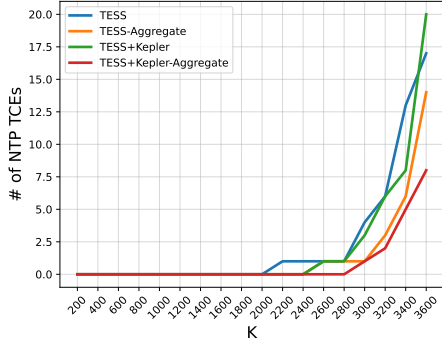
Table 8. Recall value of ExoMiner++ for photometric disposition.

Training	Test	Strategy	FP							
			VPC+	VPC-	VPC	PC	NEB	NPC	BEB	EB
TESS	TESS	Individual	0.636	0.976	0.877	0.934	0.932	0.478	1.000	0.960
		Aggregate	0.795	0.976	0.872	0.934	0.934	0.337	1.000	0.952
TESS+Kepler	TESS	Individual	0.636	0.976	0.877	0.934	0.939	0.533	0.976	0.952
		Aggregate	0.795	0.976	0.888	0.930	0.937	0.424	1.000	0.952

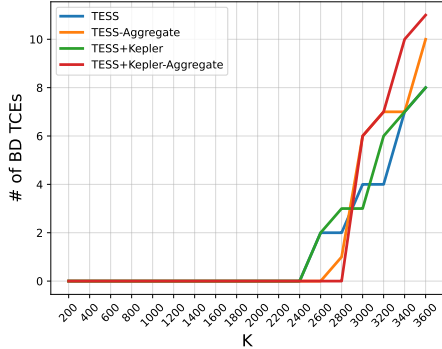
**Figure 16.** Precision@ k for the top k TCEs for different values of k and different models.

that gets into our labels are the confident ones, i.e., KP, CP, and FP.

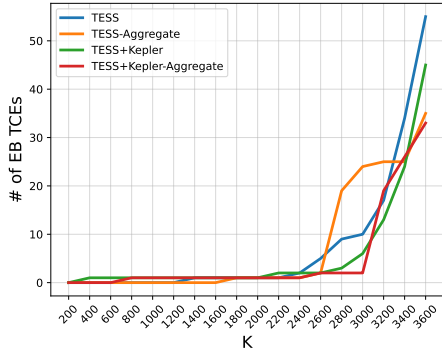
With the exception of the NPC sub-category, multi-sector aggregation performs as well as or better than its individual counterpart. For NPC, even the best model (i.e., TESS+Kepler-Individual) demonstrates very low recall. This is primarily due to the challenges of identifying background transits in TESS, which are exacerbated by its large pixel size, wide field of view, short observation windows, and the characteristics of its target stars. Many of these NPC background transits are located within 1 arcsecond of the target star. Furthermore, the uncertainty in difference imaging is greater in TESS compared to Kepler, due to systematic factors such as pointing errors. We will revisit this issue in Section 6.7, where we summarize why ExoMiner++ performs better on Kepler than on TESS. The classifier also struggles



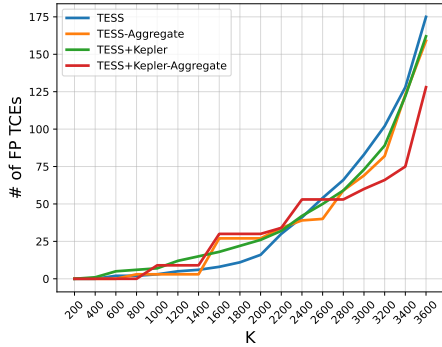
(a) NTPs



(b) BDs

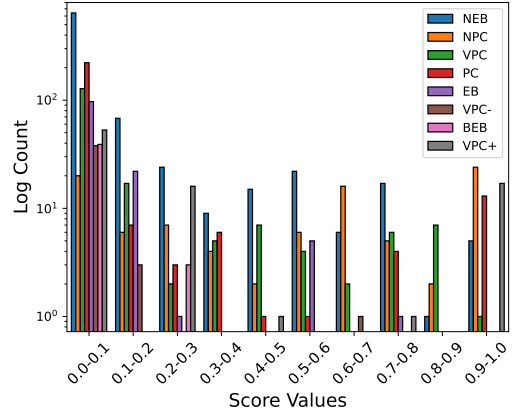


(c) EBs

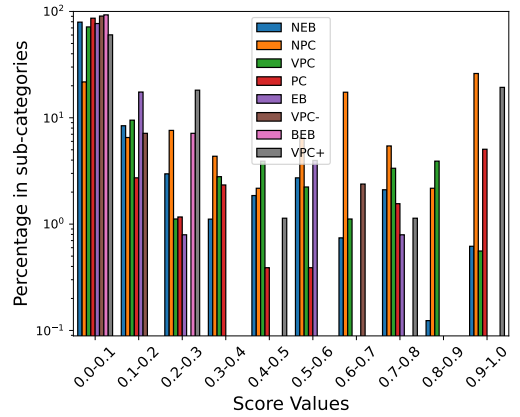


(d) FPs

Figure 17. Number of non-planets in the top k TCEs as ranked by ExoMiner++ using TESS+Kepler-Aggregate strategy.



(a) Photometric Subcategories Count



(b) Photometric Subcategories Percentage

Figure 18. Score histograms of different subcategories in photometric disposition.

with the VPC+ category, which we discuss further in Section 6.6.2.

To further examine the model’s behavior on these subcategories, we plotted the score histogram in Figure 18. These histograms reveal that ExoMiner++ not only performs inaccurately on the NPC category but also shows significant uncertainty in classifying these cases, even when the model’s disposition is correct (FP), i.e., score < 0.5. Beyond the NPC class, the model also displays generally low confidence⁸ in classifying other subcategories, such as VPC+, PC, and VPC. This is likely because photometric data alone is insufficient for effective labeling of these subcategories, which receive FP labels based on their spectroscopic disposition.

6.6.2. Spectroscopic Disposition

The spectroscopic disposition includes 23 working labels and 18 final labels. As with the photometric dispo-

⁸ Scores are distributed between 0 and 1.

Table 9. Labels description of ExoFOP’s spectroscopic disposition for FP ExoFOP master disposition. Only labels with more than 30 TCEs assignment are shown.

	nmb	Name	Description	Count
1	CRV	Cleared RV	No significant RV variations detected, but expected semi-amplitude is below current sensitivity	39
2	RR	Rapid Rotator	Rapid rotator with too much rotation for DT (generally blindly assigned if $V_{rot} > 100$ km/s)	37
3	SB1	Spectroscopic Binary 1	Single-lined spectra showing in-phase RV variation too large to be caused by a planet (e.g. only two spectra at opposite quadratures).	49
4	SEB1	Spectroscopic EB1 with orbital solution	Single-lined orbital solution with a period and epoch that match the transit ephemeris.	240
5	SB2	Spectroscopic Binary 2	Double-lined spectra moving in phase with the photometric orbit (e.g two opposite quad. spectra).	32

Table 10. Recall values of ExoMiner++ for spectroscopic dispositions.

Training	Test	Strategy	FP				
			CRV	RR	SB1	SEB1	SB2
TESS	TESS	Individual	0.872	1.000	0.959	0.796	0.969
		Aggregate	0.821	1.000	0.939	0.758	1.000
TESS+Kepler	TESS	Individual	0.872	1.000	0.980	0.796	1.000
		Aggregate	0.821	1.000	1.000	0.771	1.000

sition, we limit our analysis to labels with more than 30 TCEs that are flagged as FP in ExoFOP. This narrows it down to 5 labels, which are listed in Table 9 with their counts. The first two rows represent working dispositions, while the remaining ones are final labels. Table 10 shows the recall of ExoMiner++ for each subcategory.

The total count here is smaller than in the photometric disposition, as more than half of the TCEs with ExoFOP FP labels lack a spectroscopic disposition. The most challenging category for the TESS+Kepler-Aggregate classifier is SEB1, where 55 out of 240 SEB1 cases were misclassified by the TESS+Kepler-aggregate model. Among these, 15 had a photometric disposition of VPC, 17 were VPC+, 18 were PC, and 5 were BEB?. This suggests that, aside from the 5 BEB? cases, which show some FP signatures in the photometric data, the remaining 51 TCEs could not be correctly classified using photometric data alone.

This also explains the poor performance on VPC+, which seems more a result of statistical chance. Although the number of SEB1-labeled VPC+, VPC, and PC TCEs is similar (15-18 instances), the overall count of VPC+ is much lower, leading to poorer performance (higher misclassification rate or lower recall).

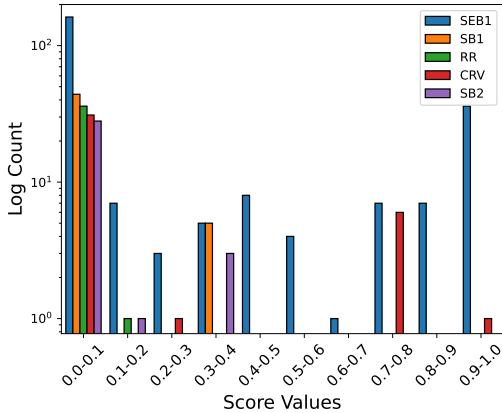
The second most difficult spectroscopic category, CRV, includes 39 TCEs, with 7 misclassified by the TESS+Kepler-aggregate model. Notably, these 7 TCEs were labeled as NEB in the photometric disposition. As

discussed in Section 6.6.1, the model also struggled with NPC, and given the significantly higher number of NEB-labeled TCEs compared to NPC, this may indicate that the poor NPC performance is coincidental mainly due to low number of total NPCs. Nonetheless, the model finds it difficult to classify NPC and NEB correctly. We discuss the difficulty of classifying background transits for TESS compared to Kepler in Section 6.7.

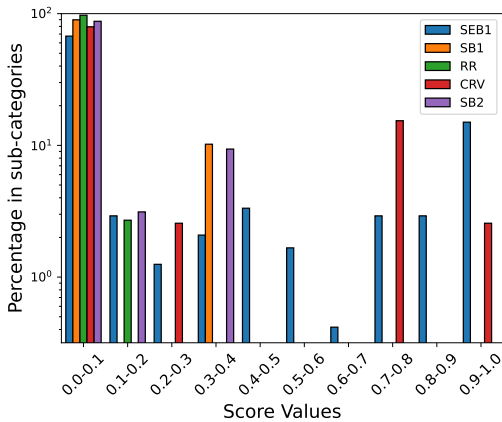
Similar to the photometric disposition, we present the score histograms of ExoMiner++ across different spectroscopic subcategories in Figure 19. Besides the model’s poor performance on SEB1, it exhibits greater uncertainty in cases it correctly classifies within spectroscopic binary categories (i.e., SEB1, SB1, and SB2). This may be because spectroscopic binaries are classified based on spectroscopic data, making photometric data alone insufficient for the model to confidently classify them, even though it performs accurately on SB1 and SB2.

6.7. Difficulty of TESS Data

As we mentioned in Section 6.4, the lower performance of ExoMiner++ on TESS compared to Kepler is not solely due to the lower SNR of TESS signals. Instead, this should be studied in terms of the TESS data quality including insufficiency of photometric data and/or imperfect label quality as we discuss below:



(a) Spectroscopic Subcategories Count



(b) Spectroscopic Subcategories Percentage

Figure 19. Score histograms of different subcategories in spectroscopic disposition.

1. **Insufficiency of photometric data:** As discussed in Section 6.6.2, there are spectroscopic subcategories, such as SEB1, that exhibit clean photometric data (i.e., without any indications of being FPs) and are assigned a non-FP label in the photometric disposition. For instance, among the 241 SEB1 TCEs, 82 are labeled as VPC, 102 as PC, 30 as VPC-, 19 as VPC+, with several other classes having fewer than 5 TCEs. This distribution indicates that photometric data alone is often insufficient to classify these TCEs as FPs. For SEB1, when compared to the photometric labels, *ExoMiner++* demonstrates better performance than human labelers relying solely on photometric data, suggesting that it can identify patterns not apparent to experts. However, as discussed in Section 6.6.2, these spectroscopic subcategories remain challenging for *ExoMiner++*.

The number of known SEB1 cases is higher in TESS compared to Kepler, primarily due to TESS’s focus

on brighter stars, which facilitates better spectroscopic follow-up. A higher percentage of brighter stars with planets naturally results in more SEB1 detections. For example, TESS SPOC TCEs corresponding to TOI 694.01 are categorized as PC in the photometric disposition and as SEB1 in the spectroscopic disposition. The photometric data shows no indications of being an FP, and specifically no signs of being an EB, as illustrated in the DV summary report in Figure 20. As noted, *ExoMiner++* can utilize trend data to detect SEB1 cases exhibiting ellipsoidal variations. However, SEB1 cases with long orbital periods, such as the ones matched to TOI 694.01, lack ellipsoidal variations, making accurate classification based on photometric data particularly challenging. For this specific SEB1 instance, there are 6 TCEs, all of which are misclassified by the model. Notably, *ExoMiner++* assigns a score of 0.92 to the TCE with the longest transit observation run, i.e., TESS SPOC TCE TIC 55383975-1-S1-65. Similar analysis can be done for other related subcategories such as SEB2, SB1 and SB2.

2. **Inconclusive diagnostic tests:** Multiple diagnostic tests have been developed to identify FPs (See [Twicken et al. 2018a](#)) originating from various sources. For instance, the weak secondary test aims to distinguish EBs from exoplanets, while the difference image test is designed to detect FPs caused by background transits. However, these tests are inherently imperfect—a challenge also encountered with Kepler. Due to the unique characteristics of the TESS mission, these tests become less reliable in certain regions of the parameter space, as discussed below.

- (a) **TCEs for exoplanets with weak secondary:** The weak secondary test is a diagnostic tool used in both Kepler and TESS missions to distinguish EBs from exoplanets. It detects faint secondary eclipses in the light curve, which are characteristic of EBs due to the secondary star’s contribution to the flux. In Kepler, the high spatial resolution and precise photometry enhance the reliability of the test, allowing clearer identification of weak secondary signals. However, in TESS, the larger pixel scale, blended light from nearby stars, and shorter observation windows reduce the test’s sensitivity and accuracy. This makes it more challenging to detect faint secondary eclipses and differentiate EBs from exoplanets

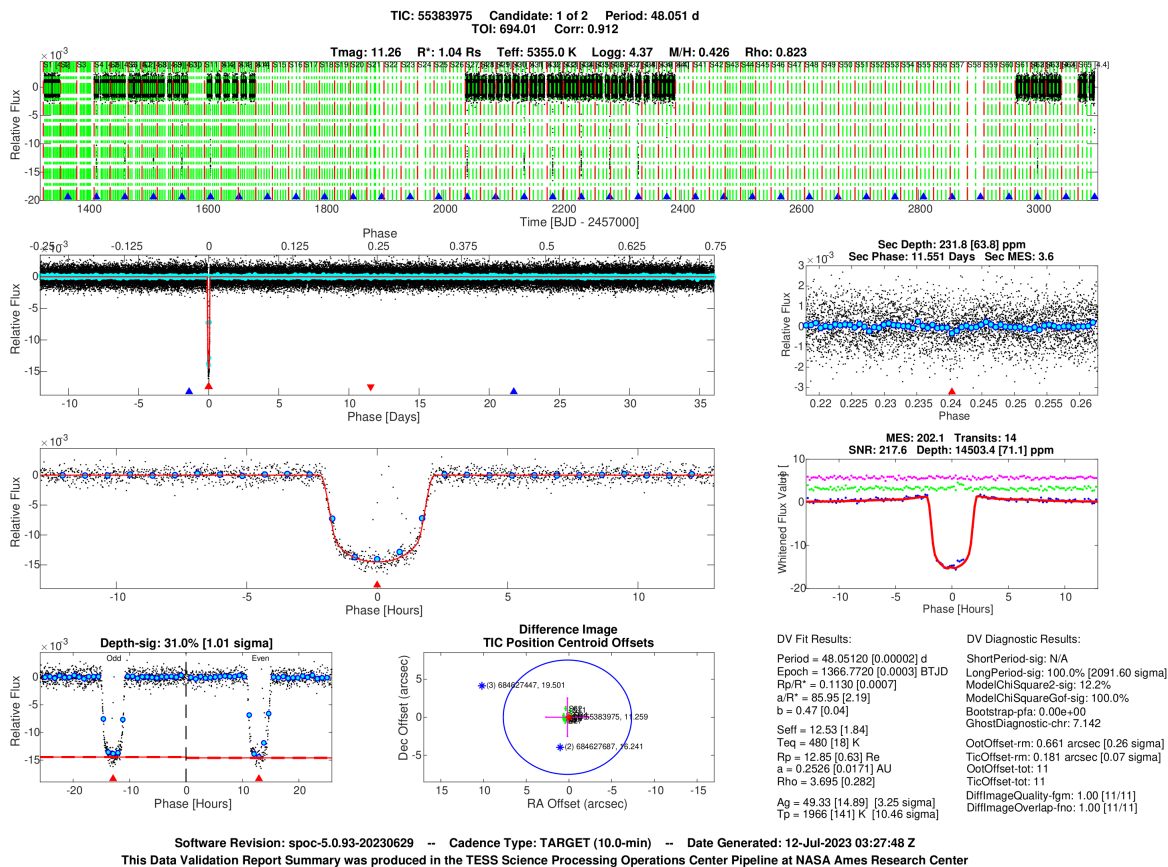


Figure 20. SPOC DV summary report for TESS SPOC TCE TIC 55383975-1-S1-65 (TOI 694.01). Photometric disposition is PC however the follow up spectroscopic indicates that this is a SEB1 indeed.

in crowded fields or regions with low signal-to-noise ratios.

The significant secondary events can also be caused by giant, short-period planets showing reflected light or thermal emission, or inadvertently by transits of other exoplanets in multi-planet systems. Experts differentiate between weak secondary events caused by EBs and those due to planets by examining the secondary geometric albedo, planet effective temperature, and MES of the secondary event (Twicken et al. 2018a; Jenkins 2020). A TCE is likely a false positive if the secondary MES exceeds the transit detection threshold 7.1, and the albedo and planet effective temperature comparisons are statistically significant. Otherwise, the test results remain inconclusive.

Our TESS dataset contains 9,217 EBs, 168 FPs, 2 BDs, and 70 exoplanets (KP+CP) TCEs with weak secondary MES > 7.1 . ExoMiner++ correctly classifies all EBs, FPs, BDs (100% recall) and 48 exoplanets (65.7%

recall) in this list⁹. Figure 21 displays scatter plots of albedo and planet effective temperature comparison statistics against weak secondary MES values for these 9457 (9,217+168+2+70) TCEs. Small values of these statistics provide limited information in distinguishing planets from EBs in the presence of weak secondary, making it difficult for the model to classify TCEs in this region accurately. However, ExoMiner++ leverages other branches to correctly classify some exoplanet TCEs with weak secondary in this region.

In some cases, weak secondary signals arise from other planets in multi-planet systems, like 4600.01 and 1339.02. Earlier ExoMiner versions, lacking the Periodogram and Flux Trend branches, often misclassified these cases. The inclusion of these branches has improved

⁹ We used TESS+Kepler-Individual for this analysis to assess model performance immediately after training, before post-processing aggregation.

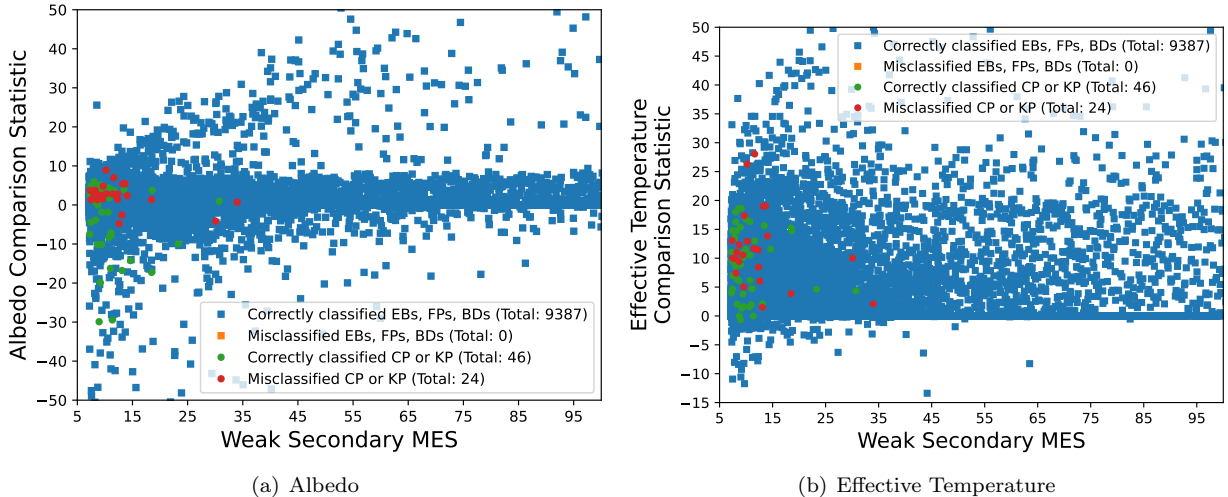


Figure 21. Albedo and planet effective temperature comparison statistics. When weak secondary MES > 7.1 , the high values of these statistics indicate a FP. However, small values do not provide much information.

accuracy for such TCEs with weak secondaries.

- (b) **Misclassified background transits:** As reported in Section 6.6.1, the recall for NPCs was slightly higher than 0.5, likely due to the difficulty of distinguishing these TCEs from planets on target stars. TESS’s larger pixel scale, necessitated by its expansive field of view, sacrifices spatial resolution compared to Kepler, which focused on a smaller field with finer spatial detail. The larger pixels in TESS increase the likelihood of blending light from nearby stars (background transits), complicating the distinction between signals originating from the target star and those from nearby sources. Additionally, some TESS fields are highly crowded, such as those along the plane of the Milky Way, further exacerbating this blending issue.

This blending significantly complicates the classification of FPs, particularly for background transits, resulting in more errors by *ExoMiner++* compared to Kepler, where the smaller pixel size allows for clearer photometric signals. For example, in the case of TESS SPOC TCE 77031413-1-S29, the difference image centroid offset points to a background transit source approximately 5.8 arcseconds from the target star—corresponding to just over 0.25 pixel in TESS but nearly 1.5 pixels in Kepler. Consequently, TESS observations are more prone to phantom stars and hierarchical systems, which further complicate the

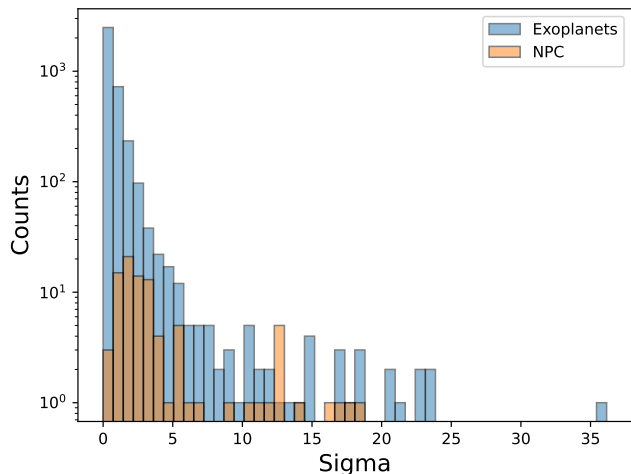
accurate classification of FPs originating from background sources.

The difference image centroid offset statistic, representing the offset divided by its uncertainty, is shown in Figure 22 for both NPC and NEB subcategories. Notably, some exoplanets have high statistic values ($\sigma > 5$), complicating the ability to learn from centroid offset alone. A number of the exoplanets with significant offsets orbit saturated stars ($T_{mag} < 7$). The change in flux during transit occurs at the top and bottom of saturation bleed trails and the difference images for such targets cannot be reliably centroided. Apparent centroid offsets on saturated stars are not typically considered when vetting TCEs.

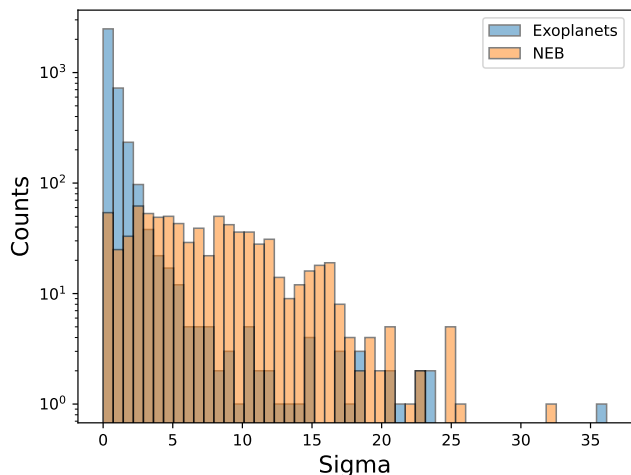
3. Incorrect ephemeris and derived parameters:

There are TCEs for which either the calculated ephemeris is incorrect or the derived parameters are inaccurate. The former issue could arise due to the short observational window of TESS, while the latter could result from inaccurate stellar parameters, among other factors. For example, TESS SPOC TCE TIC 337129672-1-S42-43 (TOI 4635.01) has an incorrect period of 49.01 days due to missing values, whereas the correct period is 12 days. The ephemeris information for such cases can be corrected using multi-sector runs.

Incorrect ephemeris information may also lead to failed ephemeris matching with TOIs, which in turn results in incorrect labeling, as discussed in the next item.



(a) NPC versus Exoplanets



(b) NEB versus Exoplanets

Figure 22. Distribution of centroid offset statistic.

4. Label quality: Due to the lack of gold-standard labels for TESS, we relied on surrogate labels from ExoFOP dispositions, the Villanova EB catalog, and TEC’s NTPs, which inherently resulted in imperfect labels. While the ExoFOP labels are highly accurate, the Villanova EB catalog, based on manual classification of photometric data, is subject to some inaccuracies. Furthermore, it is important to note that the Villanova EB catalog was constructed using only the first two years of TESS data, and with additional data now available, some dispositions may change. Our model misclassified 15 EBs (37 TCEs) out of 2,557 EBs (12,738 TCEs) from this catalog. In communication with the authors of Prša et al. (2022), they acknowledged a higher level of label noise in their catalog.

We identified five TESS SPOC TCEs—165987272-1-S14-50, 55092869-1-S9, 309792357-1-S1-13, 309792357-1-S1-39, and 309792357-1-S1-36—that were labeled as EBs due to failed ephemeris matching with a known TOI and the sequential nature of our labeling process. Using period matching alone, we determined that the first two are KPs, while the remaining three are CPs. Notably, *ExoMiner++* correctly classified all five cases.

Similarly, TEC’s vetting process is not perfect and is subject to labeling errors. For instance, we found TESS SPOC TCEs—280031353-1-S14-26, 288636342-1-S25, and 71347873-1-S20—that were labeled as NTPs due to failed ephemeris matching. These TCEs are actually PCs in ExoFOP and *ExoMiner++* classifies them as planets.

Moreover, incorrect periods, such as those being twice or half the true period of a planet, can also lead to misclassification, thereby lowering recall values. The label noise in our datasets not only complicates a thorough evaluation of model performance but can also mislead model training due to systematic errors present in the Villanova EB catalog and TEC.

6.8. Comparison with Existing TESS Classifiers

In Section 2.1, we discussed how various existing classifiers can be regarded as different instances of the machine learning classification framework presented in Figure 1, emphasizing that these classifiers primarily differ in the number and utilization of diagnostic tests they are capable of leveraging. In our previous work (Valizadegan et al. 2022), we quantitatively compared *ExoMiner* with several existing classifiers on Kepler and demonstrated that the incorporation of novel diagnostic tests and the design of *ExoMiner* led to significantly improved performance.

Aside from the work by Tey et al. (2023), which integrates some new diagnostic tests, the classifiers employed for TESS (Yu et al. 2019; Osborn et al. 2020) are largely adaptations of those developed for Kepler. As such, we anticipate similar conclusions for TESS. However, performing a quantitative comparison between *ExoMiner++* and the classifier proposed by Tey et al. (2023) is challenging for several reasons. First, their source code is not publicly available, limiting direct evaluation. Second, a comparison based on their reported results provides limited insights due to fundamental differences in their classification tasks and datasets. Specifically:

1. The authors in Tey et al. (2023) trained and evaluated their classifier on a dataset constructed through manual visual inspection of photometric data. As we demonstrated in Section 6, there are scenarios where pho-

tometric data may appear flawless, yet follow-up studies reveal their FP nature. This implies that their training and evaluation process could have been misled by incorrect labels.

2. Their classification task involves distinguishing periodic eclipsing signals (encompassing planetary transits and non-contact EBs, both on- and off-target) from contact EBs, single-transit events, and non-transiting phenomena (e.g., stellar variability and instrumental noise). This task is a “relaxed” version of the classification task addressed in our work, as it groups planetary transits with other periodic signals.

3. Their dataset consists of TCEs detected by the Quick-Look Pipeline (QLP) from TESS full-frame image (FFI) data. To compare the datasets, one would need to identify the subset of TCEs from the two pipelines that correspond to the same events and obtain the scores generated by the classifier in Tey et al. (2023), which are not publicly available.

Out of curiosity, we conducted ephemeris matching between the publicly available dataset used in Tey et al. (2023) and our dataset. This matching yielded approximately 3.2k shared TCEs, representing a small fraction of our dataset. This limited overlap can be attributed to the fact that the authors in Tey et al. (2023) focused on a restricted selection of QLP TCEs from the first three years of the TESS Mission. Moreover, only a fraction of their dataset (10%) was allocated for testing, further reducing the subset of TCEs available for performance comparison.

6.9. Ablation Experiments for New ExoMiner++ Branches

As described in Section 3, we have introduced five new branches to the ExoMiner architecture when designing the new model ExoMiner++. These branches were added to provide the model with additional information that, according to SMEs and our understanding of the challenges and specifics of the TESS Mission, could be leveraged to improve the performance of the model. To substantiate these hypotheses, we conducted ablation experiments in which we investigated the changes in model’s performance due to the inclusion of these new branches. We started by training and evaluating a baseline model (Flux) that uses only the transit- and full-orbit-view flux branches. For each new branch, we trained and evaluated a model that consisted of the branches found in the baseline model plus the branch of interest. Similar to the results obtained for the full ExoMiner++ model in Section 6.4, we used the same setup described in Section 5, and trained and evaluated all models on TESS data. The metrics were computed for the ‘Individual’ strategy

because we were interested in studying the direct effect of these branches on the model just after the training without any post-processing.

Table 11 shows the performance metrics for each of these models and their recall values (for a threshold of 0.5) for the multiple subclasses. All models except for the ‘Momentum Dump’ model show an increase in the PR AUC when compared to the baseline model, suggesting that all these branches contribute to an overall better separation between planet and non-planet TCEs.

The top performing branch is ‘Flux Trend’, demonstrating that providing information about the fitted trend is useful to the model. We hypothesized that these data might contain other signals besides the transit event that occur at the time scale of the detected orbital period. As mentioned previously, examples of such cases include ellipsoidal variations of short-period EBs such as the one shown in Figures 4 and 10. In this particular case, the baseline model classified incorrectly this EB as a planet with a high score of 0.88. On the contrary, the ‘Flux Trend’ model, which has access to information about the ellipsoidal variations through the phase-folded trend flux time series, assigned a score of 0.09 to this TCE, correctly identifying it as a non-planet.

Focusing on the FP subclasses, the ‘Periodogram’ branch exhibits the highest recall for the brown dwarf subset, leading to three fewer misclassifications relative to the baseline model. This suggests that frequency domain information can be useful to distinguish these objects from their planet counterparts. However, given the small sample size of this subclass, this conclusion should be taken with caution.

For the EB subclass, both ‘Difference Image’ and ‘Periodogram’ models show the highest increase in recall. While the flux trend data can provide information about a subpopulation of EBs with visible ellipsoidal variations, it seems that there are more information conveyed in the pixel data as well as in the frequency domain that helps in the correct classification of these TCEs.

For the FP subclass, the ‘Difference Image’ exhibits the highest recall. These results are studied in more detail below when discussing the performance using photometric dispositions for this subclass.

Finally, although the baseline model already shows a high recall for the NTP subclass, the ‘Unfolded Flux’ model shows the highest recall for this subclass among all models evaluated in this experiment. This is expected because the main reason for the inclusion of unfolded flux data is to study the inconsistency of the transits over different periods, which is mainly used to identify NTP transits.

Table 11. Results of ablation experiments for the new branches added to **ExoMiner++**. Models were trained and evaluated only on TESS data. The best performer is highlighted in bold.

Model	Binary results				Recall for subclasses					
					Exoplanets		Non-planets			
	Precision & Recall	PR AUC	ROC AUC	Accuracy	KP	CP	BD	EB	FP	NTP
Flux (baseline)	0.811 & 0.863	0.897	0.988	0.978	0.910	0.816	0.656	0.985	0.746	0.997
Difference Image	0.850 & 0.831	0.904	0.989	0.980	0.891	0.772	0.719	0.989	0.801	0.999
Flux Trend	0.835 & 0.876	0.923	0.991	0.981	0.917	0.835	0.656	0.986	0.772	0.998
Periodogram	0.851 & 0.842	0.911	0.990	0.980	0.893	0.793	0.750	0.989	0.790	0.999
Unfolded Flux	0.839 & 0.866	0.913	0.990	0.981	0.900	0.832	0.625	0.987	0.754	1.000
Momentum Dump	0.809 & 0.867	0.897	0.989	0.978	0.916	0.818	0.656	0.984	0.738	0.998

Table 12. Recall for photometric and spectroscopic disposition using results from ablation experiments conducted for the new branches added to **ExoMiner++**. Models were trained and evaluated only on TESS data.

Model	FP Photometric								FP Spectroscopic				
	VPC+	VPC-	VPC	PC	NEB	NPC	BEB	EB	CRV	RR	SB1	SEB1	SB2
Flux (baseline)	0.432	0.976	0.749	0.899	0.743	0.304	0.905	0.976	0.769	0.946	0.959	0.729	0.969
Difference Image	0.500	0.976	0.777	0.922	0.821	0.337	0.952	0.984	0.872	0.946	0.959	0.746	0.938
Flux Trend	0.523	0.976	0.821	0.911	0.756	0.283	0.952	0.984	0.795	0.973	0.939	0.792	0.969
Periodogram	0.648	0.976	0.888	0.914	0.759	0.315	0.952	0.976	0.846	0.919	1.000	0.808	0.938
Unfolded Flux	0.443	0.976	0.777	0.918	0.752	0.283	0.929	0.960	0.744	0.946	0.918	0.729	0.938
Momentum Dump	0.443	0.976	0.760	0.895	0.731	0.239	0.905	0.968	0.590	0.946	0.959	0.704	0.906

Table 12 shows the recall values for different types of ExoFOP FPs based on their photometric and spectroscopic dispositions. Some of these disposition categories have a small set of TCEs (e.g., BEB, CRV, RR, SB1, and SB2), and so the results should be interpreted with caution. The analysis of the results for the photometric dispositions shows that the ‘Difference Image’ branch is particularly effective at improving the classification of background objects (i.e, NEBs and NPCs), leading to 66 fewer misclassifications out of a total of 900 background objects TCEs. As expected, a significant fraction of these objects shows a clear transit source offset in the difference image data which can be used by the model to infer that these transiting events are not happening on the target. Furthermore, the ‘Difference Image’ branch improves the recall for PC subclass, which suggests that, although these planet candidates do not have any follow-up photometric observations (or if they do, they are inconclusive), the pixel data that are processed through the ‘Difference Image’ branch leads the model to correctly classify more of these instances as non-planet TCEs.

The results for the EB subclass suggest that adding the ‘Difference Image’ and ‘Flux Trend’ branches leads to performance improvement for this subcategory. In a similar fashion, these two branches and the ‘Periodogram’ seem to improve the recall for BEBs. However, given the size of these two sets and the difference in recall compared to the baseline model, these findings need to be taken with caution.

The ‘Periodogram’ branch also reveals itself significantly effective in improving the classification of VPC+ and VPC subclasses. Interestingly, all models obtain the same recall as the baseline for VPC- subclass. According to the definition in Table 7, VPC- are transiting events that have been confirmed by SG1 to occur within the target star aperture in follow-up observations, but there are known stars contaminating the aperture that are bright enough to be potential sources of the transit. Given this, providing additional difference image data to the model is not enough evidence to determine whether the transiting event occurs on-target, which explains why we see similar performance for this subset of TCEs

across all branch models, including the ‘Difference Image’ model which was designed to help distinguishing detection on neighboring stars. This is a known limitation of **ExoMiner++** model, and one that we plan to address in future work.

As of now, the model does not have information on nearby stars that potentially contaminate the aperture. We hypothesize that an improved representation of the difference image with additional channels that provide the model information about the location of known background stars in the postage stamp and their brightness values can be leveraged by the model to decrease the scores for crowded field scenarios, thus improving the quality of vetting catalogs produced using **ExoMiner++** and the validation and follow-up of its planet candidates.

For the VPC subclass, the ‘Periodogram’ data seems to carry useful information that is employed by the model to improve its sensitivity to these observations relative to the baseline model. According to the definition in Table 7, these events have been verified to occur within the target star aperture and no known stars in the vicinity are bright enough to cause the detection. Nonetheless, based on the performance of the ‘Periodogram’ branch model, there is some signature in the frequency domain that makes the model more assertive in classifying these events as false positives. In the future we will conduct explainability studies to investigate which frequencies in the periodogram contribute the most to the model’s score for this and other sets of objects.

Regarding the spectroscopic dispositions of ExoFOP’s FP TCEs, this analysis shows that the ‘Periodogram’ branch can be effective at distinguishing some types of spectroscopic EBs, including SEB1, which is the largest spectroscopic category (see Table 12), and SB1. Again, the results for SB1 and SB2 should be studied with caution given their smaller sample size. All other branches do not seem to convey any meaningful information that can help the model correctly classify these observations. Rapidly rotating stars (RR subcategory) can induce transit-like events in the photometry data. This type of stellar variability leads to the creation of FP TCEs, especially if these stars have spots. The results in Table 12 suggest that the ‘Flux Trend’ branch model helps in the classification of RR TCEs, while all other branches do not outperform the baseline. Despite being a small set of examples, the trend data might capture some of the variability induced by these objects in the light curve time series. As for the CRV disposition, the results for the ‘Difference Image’ and ‘Periodogram’ models suggest that these branches might help the model in correctly identifying these events. This is interesting since in these cases no significant radial velocity variations were de-

tected, but the expected value for the semi-amplitude is below the sensitivity threshold. However, we refrain from making final conclusions until we have a larger number of TCEs in this category and a better sense of how these data can help.

All these results point to the usefulness of the new branches added to **ExoMiner++** to boost the performance of the model. The only exception to this is the ‘Momentum Dump’ branch. The design and inclusion of this branch had been motivated by the desire to provide information to the model about TCEs created by flux level artifacts associated with momentum dump events. However, most of such cases are effectively filtered by the SPOC transit search pipeline¹⁰, and so it is difficult to find a set of momentum dump TCEs in the data. This means that the model does not see many examples that are relevant to this branch during training, and at the same time it becomes difficult to evaluate the model on such a small sample and provide meaningful statistics.

We note that our ablation experiment does not account for higher-order interactions among branches (e.g., simultaneously adding the ‘Difference Image’ and ‘Periodogram’ branches to the baseline model) due to the increased combinatorial complexity and resource demands. In future work, we plan to perform an in-depth explainability analysis to gain deeper insights into the model’s behavior. These insights could not only inform the design of improved models but also provide valuable information to researchers seeking to understand and utilize the model’s predictions.

7. BUILDING A VETTING CATALOG FOR TESS 2-MIN DATA

One of the key outcomes of this study is the construction of a comprehensive vetting catalog for TESS 2-minute cadence data using **ExoMiner++**. This catalog serves as a curated resource of transit-like signals, classifying them as likely exoplanets or non-planets. Leveraging the advanced classification capabilities of **ExoMiner++**, the catalog aims to provide the TESS and broader exoplanets community with a reliable dataset for follow-up investigations and population studies.

As detailed in Section 4.1, the labeling process assigned labels to 57,162 TCEs out of a total of 204,729 TCEs, leaving 147,567 unlabeled TCEs, referred to as unknowns (UNKs). To classify these UNKs, we applied the ten TESS+Kepler **ExoMiner++** models trained using 10-fold cross-validation and averaged their scores for final classification. Table 14 presents the labels and

¹⁰ This occurred early in the TESS mission, but the SPOC pipeline implemented de-emphasis weights to mitigate such occurrences.

detailed scores for these 147,567 UNK TCEs, of which **ExoMiner++** identified 7,330 as planet candidates, based on the average score of 10 models and the application of aggregation strategy (Section 6.3) on the top (last column of Table 14).

Table 15 presents the dispositions and scores for the TOIs matched to the unknown TCEs, using the aggregate strategy to obtain a single disposition/score for the case of multiple TCEs corresponding to the same TOI. Out of 2,806 matched TOIs, **ExoMiner++** classified 1,868 as planet candidates.

It is important to note that both Table 14 and Table 15 include two distinct columns for TFOPWG dispositions. The first column corresponds to data downloaded in January 2024, which was used to construct the dataset for training and evaluating **ExoMiner++**. The second column corresponds to the TFOPWG table downloaded during the final phase of this work in December 2024, which was utilized to build the vetting catalog.

Over time, some uncertain TFOPWG dispositions (i.e., PC, APC, and FA) have been updated to more certain dispositions such as CPs and FPs, as reported in Table 13.

Table 13. The ExoFOP label changes over an 11-month period, reported in terms of the number of TCEs. The numbers in parentheses represent the corresponding number of TOIs. The labels of some TCEs changed from uncertain labels to certain labels CP and FP.

		Jan 2024 labels		
		PC	APC	FA
Dec 2024 labels	PC	7990 (2423)	0 (0)	0 (0)
	FA	1 (1)	5 (1)	77 (43)
	APC	98 (23)	958 (240)	0 (0)
	FP	55 (27)	87 (13)	0 (0)
	CP	151 (32)	0 (0)	0 (0)

The difference between these two TFOPWG tables provides an opportunity to compare the performance of the **ExoMiner++** TCE catalog with the TOI TFOPWG uncertain dispositions, such as PC, APC, and FA, and to understand the expected value of **ExoMiner++** over time. However, it is important to note that this analysis should be interpreted with caution due to the small sample size of changes between January 2024 and December 2024.

The December 2024 TFOPWG table has 151 new CP TCEs and 142 new FP TCEs, that were labeled with uncertain labels (PC, APC, and FA) in January 2024 table. These TCEs were labeled as unknown in our data set and were not used for training or evaluation of the model. We can now use them to provide some insight into what to ex-

pect from **ExoMiner++** over time. **ExoMiner++** correctly classified 147 out of 151 CP TCEs and 95 out of 142 FP TCEs (precision=0.76, recall=0.97). In comparison, the TFOPWG January 2024 dispositions labeled all 151 CPs and 55 FPs as PCs, with the remaining FPs labeled as APC, resulting in precision=0.50, recall=1.0. This demonstrates that **ExoMiner++** significantly enhances the efficiency of the planet search process by providing more accurate classifications, achieving higher precision at the modest cost of recall.

Finally, we were interested in identifying whether there are new TOIs discovered by **ExoMiner++**. Out of a total of 7,330 UNK TCEs classified as PC, 6,322 TCEs were already matched to 1,868 existing TOIs using the procedure described in Section 4.1, leaving 1,008 TCEs without a TOI match. However, as discussed earlier, our ephemeris matching process may occasionally fail to associate a TCE with known TOIs. Furthermore, there are Community TOIs (CTOIs)¹¹ that we should exclude from consideration.

To address this, we performed an aggressive period matching by removing any TCEs for a target star that had a TOI or CTOI with a similar period, using a 1% threshold for matching ($|P_{\text{TOI}} - P_{\text{TCE}}| < 0.01 \times P_{\text{TOI}}$). This process excluded 512 TCEs matched to existing TOIs and 69 matched to existing CTOIs, leaving 427 new TCEs classified as PC by **ExoMiner++**.

Subsequently, we conducted another level of period-based ephemeris matching among these 427 TCEs, resulting in a total of 288 unique events. To generate a more conservative list of CTOIs, we applied two additional vetoes: (1) ensuring that all 10 models trained using 10-fold cross-validation classified the TCEs with the longest sector run of these events as PC (score > 0.5), and (2) requiring that each TCE exhibited at least three observed transits. This refinement resulted in 91 unique events that are potentially new CTOIs.

The SMEs on the team then manually examined these 91 potential CTOIs, ultimately rejecting 41 due to various reasons, the majority being related to target stars that were determined to be duplicates, or artifacts in TIC-8. This left us with 50 new CTOIs, which are reported in Table 16.

By making these catalogs publicly available, we aim to support ongoing and future studies, ranging from follow-up investigations of the most promising candidates to detailed atmospheric characterizations and population-level analyses of exoplanets. This catalog represents a significant advancement in the automated vetting of

¹¹ https://exofop.ipac.caltech.edu/tess/view_ctoi.php

TESS 2-minute cadence data, bridging the gap between detection and validation in the search for worlds beyond our solar system.

Table 14. Scores and dispositions of TESS+Kepler-Aggregation model for UNK TCEs. This table describes the available columns. The full table is available online.

Column	Description
uid	Unique ID that includes TIC ID, planet number, and sector run
target_id	TIC ID
tce_plnt_num	TCE planet number
toi	TOI number
tce_period	TCE period
tce_duration	TCE duration
tce_prad	TCE planet radius (Earth Radii)
mes	TCE MES
TFOPWG Disposition (January 2024)	One of multiple TFOPWG Dispositions downloaded in January 2024 if available for a TCE
TFOPWG Disposition (December 2024)	One of multiple TFOPWG Dispositions downloaded in December 2024 if available for a TCE
score_fold.i	for $i \in [0, 9]$, this is the score of ExoMiner++ model trained for fold i
ExoMiner++ score	Average score of 10 ExoMiner++ models
ExoMiner++ score std	Standard deviation of scores of 10 ExoMiner++ models
ExoMiner++ aggregate score	Aggregate scores computed on the top of tess-individual mean score
ExoMiner++ label	‘PC’ if ‘ ExoMiner++ score’ > 0.5, ‘FP’ otherwise
ExoMiner++ aggregate label	‘PC’ if ‘ ExoMiner++ aggregate score’ > 0.5, ‘FP’ otherwise
DV full report	The URL to the DV full report in the MAST
DV summary report	The URL to the DV summary report in the MAST
DV mini report	The URL to the DV mini report in the MAST

8. CONCLUSION

In this work, we introduced **ExoMiner++**, a machine learning-based model tailored for the classification and ranking of transit signals in TESS 2-minute cadence data. By leveraging transfer learning from Kepler, **ExoMiner++** exhibits robust performance in distinguishing planetary signals from false positives across a variety of challenging scenarios.

Table 15. Scores and dispositions of TESS+Kepler-Aggregation model for TOIs that could be matched to TCEs using ephemeris matching procedure in 4.1. This table describes the available columns. The full table is available online.

Column	Description
uid	Unique ID that includes TIC ID, planet number, and sector run
target_id	TYIC ID
tce_plnt_num	TCE planet number
toi	TOI ID
tce_period	TCE period
tce_duration	TCE duration
tce_prad	TCE planet radius (Earth Radii)
mes	TCE MES
TFOPWG Disposition (January 2024)	One of multiple TFOPWG Dispositions downloaded in January 2024 if available for a TOI
TFOPWG Disposition (December 2024)	One of multiple TFOPWG Dispositions downloaded in December 2024 if available for a TOI
score_fold.i	for $i \in [0, 9]$, this is the score of ExoMiner++ model trained for fold i
ExoMiner++ score	Average score of 10 ExoMiner++ models
ExoMiner++ score std	Standard deviation of scores of 10 ExoMiner++ models
ExoMiner++ label	‘PC’ if ‘ ExoMiner++ score’ > 0.5, ‘FP’ otherwise
DV full report	The URL to the DV full report in the MAST
DV summary report	The URL to the DV summary report in the MAST
DV mini report	The URL to the DV mini report in the MAST

The model outputs both discrete classifications of TCEs as planets or non-planets and a continuous confidence score, providing a dual utility. This enables not only precise classification but also the development of a ranking-based vetting catalog for TESS 2-minute data. Such a catalog serves as a valuable resource for the astronomical community, streamlining the identification and prioritization of promising planetary candidates while minimizing the need for manual vetting.

Our analysis underscores several inherent challenges in classifying TESS data, including label noise, the effects of larger pixel sizes, crowded stellar fields, and systematic uncertainties. Despite these challenges, **ExoMiner++** demonstrates exceptional performance, particularly in addressing difficult subcategories. Its success stems from

Table 16. List of 50 new CTOIs.

Number	UID	Target ID	Planet Number	Period	Duration	Planet Radius (Earth Radii)	MES	ExoMiner++ Score
1	55655482-1-S14-60	55655482	1	3.96	0.11	13.58	229.30	0.993
2	207109417-1-S1-36	207109417	1	0.29	0.02	1.71	12.96	0.984
3	292547242-1-S39	292547242	1	7.14	0.06	7.09	10.15	0.983
4	46298321-1-S42-46	46298321	1	1.11	0.04	6.08	18.05	0.981
5	1715469667-1-S14-55	1715469667	1	6.50	0.23	7.85	103.10	0.976
6	233535738-2-S14-60	233535738	2	7.93	0.15	2.36	10.24	0.976
7	158561812-1-S14-55	158561812	1	3.69	0.03	6.08	9.59	0.973
8	241514551-2-S1-65	241514551	2	8.12	0.07	6.14	8.48	0.972
9	96202086-3-S14-60	96202086	3	0.63	0.02	0.89	10.09	0.970
10	396572386-1-S58	396572386	1	4.68	0.11	12.23	62.59	0.965
11	198178859-1-S14-55	198178859	1	7.31	0.14	1.34	8.04	0.956
12	66013259-1-S59	66013259	1	2.92	0.07	12.43	10.41	0.942
13	417829948-1-S14-50	417829948	1	8.95	0.12	2.17	7.41	0.942
14	224603921-1-S14-55	224603921	1	26.35	0.20	1.39	8.68	0.941
15	459928783-1-S14-50	459928783	1	11.07	0.11	2.96	8.53	0.936
16	309155144-1-S38	309155144	1	4.51	0.03	2.06	7.26	0.934
17	51079186-1-S13	51079186	1	5.29	0.11	2.75	10.18	0.928
18	270174158-1-S1-13	270174158	1	8.73	0.15	2.36	7.80	0.922
19	423454257-1-S1-65	423454257	1	12.60	0.11	1.28	8.18	0.917
20	193607307-1-S14-55	193607307	1	3.62	0.15	0.77	7.28	0.906
21	18018496-1-S14-50	18018496	1	6.25	0.09	1.95	8.25	0.906
22	96966437-1-S55	96966437	1	3.81	0.11	15.40	76.58	0.906
23	18068144-1-S14-50	18068144	1	14.25	0.15	3.05	8.28	0.890
24	5892614-1-S42-46	5892614	1	20.44	0.33	23.02	15.65	0.874
25	61710094-1-S1-36	61710094	1	1.84	0.06	1.91	8.58	0.873
26	20291519-1-S14-55	20291519	1	0.83	0.02	2.61	12.09	0.842
27	390201695-1-S14-26	390201695	1	10.88	0.19	3.32	10.38	0.839
28	239633605-1-S14-60	239633605	1	3.96	0.15	1.59	7.28	0.836
29	301969042-1-S41	301969042	1	0.88	0.09	3.10	8.27	0.829
30	258776466-1-S14-55	258776466	1	7.41	0.08	1.59	11.06	0.828
31	176218374-1-S1-46	176218374	1	13.28	0.12	2.16	7.28	0.827
32	117357458-1-S42-46	117357458	1	6.92	0.15	9.28	8.20	0.809
33	354103297-1-S17	354103297	1	2.78	0.11	3.59	9.55	0.784
34	147476037-1-S60	147476037	1	4.24	0.16	4.27	7.32	0.777
35	178645961-1-S1-65	178645961	1	23.53	0.57	0.90	8.22	0.756
36	97931135-1-S1-65	97931135	1	2.49	0.11	1.05	9.73	0.748
37	402313695-1-S1-46	402313695	1	14.86	0.12	1.89	8.74	0.741
38	278862747-1-S1-65	278862747	1	13.58	0.21	4.02	11.60	0.734
39	297262361-1-S14-60	297262361	1	7.78	0.14	0.79	8.56	0.732
40	295679570-1-S50	295679570	1	6.37	0.12	2.81	7.32	0.706
41	35228717-1-S42-46	35228717	1	11.68	0.19	4.29	8.52	0.687
42	257816591-1-S42-43	257816591	1	5.27	0.05	8.85	8.83	0.682
43	363459149-1-S42-46	363459149	1	18.24	0.12	18.20	124.83	0.682
44	63068354-1-S14-55	63068354	1	20.49	0.18	2.94	14.63	0.679
45	370977908-1-S1-65	370977908	1	17.09	0.22	2.39	7.32	0.678
46	196778101-1-S17	196778101	1	2.78	0.11	3.94	8.14	0.666
47	191702922-1-S58	191702922	1	3.32	0.14	3.52	7.37	0.642
48	410393041-1-S1-65	410393041	1	26.84	0.10	2.58	8.91	0.640
49	302609939-1-S1-46	302609939	1	49.62	0.13	2.04	8.96	0.635
50	274212635-1-S31	274212635	1	0.24	0.02	3.79	17.53	0.586

a combination of transfer learning and innovative diagnostic tests, enhanced by advanced deep learning-based feature extraction capabilities.

ExoMiner++ marks a significant advancement in automated exoplanet discovery, complementing human expertise with scalable, data-driven methodologies. Future work could extend this approach to other data sources, such as TESS Full-Frame Images (FFIs), and improve the handling of blended signals and misclassified subcategories. These advancements will pave the way toward

fully automated validation of TESS exoplanets. As TESS continues to deliver an abundance of observational data, tools like **ExoMiner++** will be pivotal in maximizing the mission’s contributions to exoplanetary science.

ACKNOWLEDGMENTS

HV and MM are supported through TESS XRP 2022 contract 22-XRP22.2-0173, NASA Academic Services Mission (NAMS) contract number NNA16BD14C as well as the Intelligent Systems Research and Development-

3 (ISRDS-3) Contract 80ARC020D00100. DC and JT are supported through NASA Cooperative Agreement 80NSSC21M0079. VK acknowledges support from the youth scientific laboratory project, topic FEUZ-2020-0038. G.N. thanks for the research funding from the Ministry of Science and Higher Education program the "Excellence Initiative - Research University" conducted at the Center of Excellence in Astrophysics and Astrochemistry of the Nicolaus Copernicus University in Toruń, Poland. The postdoctoral fellowship of KB is funded by F.R.S.-FNRS grant T.0109.20 and by the Francqui Foundation.

We would like to thank multiple people who directly or indirectly contributed to this work. This paper includes data collected by the Kepler mission and obtained from the MAST data archive at the Space Telescope Science Institute (STScI). Funding for the Kepler mission was provided by the NASA Science Mission Directorate. Resources supporting this work were provided by the NASA High-End Computing (HEC) Program through the NASA Advanced Supercomputing (NAS) Division at Ames Research Center for the production of the Kepler SOC and the TESS SPOC data products and for training our deep learning model, **ExoMiner++**.

Funding for the TESS mission is provided by NASA's Science Mission Directorate. KAC and CNW acknowledge support from the TESS mission via subaward s3449 from MIT. This paper made use of data collected by the TESS mission and are publicly available from the Mikulski Archive for Space Telescopes (MAST) operated by the Space Telescope Science Institute (STScI). We acknowledge the use of public TESS data from pipelines at the TESS Science Office and at the TESS Science Processing Operations Center. This work makes use of observations from the LCOGT network. Part of the LCOGT telescope time was granted by NOIRLab through the Mid-Scale Innovations Program (MSIP). MSIP is funded by NSF. This paper is based on observations made with the Las Cumbres Observatory's education network telescopes

that were upgraded through generous support from the Gordon and Betty Moore Foundation. This paper is based on observations made with the MuSCAT3/4 instruments, developed by the Astrobiology Center (ABC) in Japan, the University of Tokyo, and Las Cumbres Observatory (LCOGT). MuSCAT3 was developed with financial support by JSPS KAKENHI (JP18H05439) and JST PRESTO (JPMJPR1775), and is located at the Faulkes Telescope North on Maui, HI (USA), operated by LCOGT. MuSCAT4 was developed with financial support provided by the Heising-Simons Foundation (grant 2022-3611), JST grant number JPMJCR1761, and the ABC in Japan, and is located at the Faulkes Telescope South at Siding Spring Observatory (Australia), operated by LCOGT. This research has made use of the Exoplanet Follow-up Observation Program (ExoFOP; DOI: 10.26134/ExoFOP5) website, which is operated by the California Institute of Technology, under contract with the National Aeronautics and Space Administration under the Exoplanet Exploration Program.

This material is based upon work supported by the NASA under Agreement No. 80NSSC21K0593 for the program "Alien Earths". The results reported herein benefitted from collaborations and/or information exchange within NASA's Nexus for Exoplanet System Science (NExSS) research coordination network sponsored by NASA's Science Mission Directorate.

This work makes use of observations from the ASTEP telescope. ASTEP benefited from the support of the French and Italian polar agencies IPEV and PNRA in the framework of the Concordia station program and from OCA, INSU, Idex UCAJEDI (ANR- 15-IDEX-01) and ESA through the Science Faculty of the European Space Research and Technology Centre (ESTEC). This research also received funding from the European Research Council (ERC) under the European Union's Horizon 2020 research and innovation program (grant agreement No. 803193/BEBOP) and from the Science and Technology Facilities Council (STFC; grant No. ST/S00193X/1).

REFERENCES

- Ansdell, M., Ioannou, Y., Osborn, H. P., et al. 2018, *The Astrophysical Journal*, 869, L7, doi: [10.3847/2041-8213/aaf23b](https://doi.org/10.3847/2041-8213/aaf23b)
- Armstrong, D. J., Gamper, J., & Damoulas, T. 2020, *Monthly Notices of the Royal Astronomical Society*, 504, 5327–5344, doi: [10.1093/mnras/staa2498](https://doi.org/10.1093/mnras/staa2498)
- Bishop, C. M. 2006, *Pattern Recognition and Machine Learning (Information Science and Statistics)* (Berlin, Heidelberg: Springer-Verlag)
- Borucki, W. J., Koch, D., Basri, G., et al. 2010, *Science*, 327, 977
- Breiman, L. 2001, *Machine Learning*, 45, 5, doi: [10.1023/A:1010933404324](https://doi.org/10.1023/A:1010933404324)
- Coughlin, J. L. 2017, KSCI-19114-001
- Cui, K., Liu, J., Feng, F., & Liu, J. 2021, *The Astronomical Journal*, 163, 23, doi: [10.3847/1538-3881/ac3482](https://doi.org/10.3847/1538-3881/ac3482)
- Falkner, S., Klein, A., & Hutter, F. 2018, in *International conference on machine learning*, PMLR, 1437–1446

- Fetherolf, T., Pepper, J., Simpson, E., et al. 2023a, *The Astrophysical Journal Supplement Series*, 268, 4, doi: [10.3847/1538-4365/acdee5](https://doi.org/10.3847/1538-4365/acdee5)
- . 2023b, *The Astrophysical Journal Supplement Series*, 268, 4
- Fukushima, K. 1969, *IEEE Transactions on Systems Science and Cybernetics*, 5, 322
- Giacalone, S., Dressing, C. D., Jensen, E. L. N., et al. 2020, *The Astronomical Journal*, 161, 24, doi: [10.3847/1538-3881/abc6af](https://doi.org/10.3847/1538-3881/abc6af)
- Guerrero, N. M., Seager, S., Huang, C. X., et al. 2021, *ApJS*, 254, 39, doi: [10.3847/1538-4365/abefe1](https://doi.org/10.3847/1538-4365/abefe1)
- Hansen, M. T., & Dittmann, J. A. 2024, *Single Transit Detection In Kepler With Machine Learning And Onboard Spacecraft Diagnostics*. <https://arxiv.org/abs/2403.03427>
- Hastie, T., Tibshirani, R., & Friedman, J. 2009, *The Elements of Statistical Learning: Data Mining, Inference, and Prediction*, Second Edition (Springer Series in Statistics)
- He, K., Zhang, X., Ren, S., & Sun, J. 2015, in *Proceedings of the IEEE international conference on computer vision*, 1026–1034
- Hornik, K., Stinchcombe, M., & White, H. 1989, *Neural Networks*, 2, 359, doi: [https://doi.org/10.1016/0893-6080\(89\)90020-8](https://doi.org/10.1016/0893-6080(89)90020-8)
- Jenkins, J. M. 2020, KSCI-19081-003
- Jenkins, J. M., McCauliff, S., Burke, C., et al. 2014, in *Formation, Detection, and Characterization of Extrasolar Habitable Planets*, ed. N. Haghighipour, Vol. 293, 94–99, doi: [10.1017/S1743921313012611](https://doi.org/10.1017/S1743921313012611)
- Jenkins, J. M., Twicken, J. D., McCauliff, S., et al. 2016, in *Society of Photo-Optical Instrumentation Engineers (SPIE) Conference Series*, Vol. 9913, *Software and Cyberinfrastructure for Astronomy IV*, ed. G. Chiozzi & J. C. Guzman, 99133E, doi: [10.1117/12.2233418](https://doi.org/10.1117/12.2233418)
- Jolliffe, I. T., & Cadima, J. 2016, *Philosophical Transactions of the Royal Society A: Mathematical, Physical and Engineering Sciences*, 374. <https://api.semanticscholar.org/CorpusID:20101754>
- Kingma, D. P. 2014, arXiv preprint arXiv:1412.6980
- Krizhevsky, A., Sutskever, I., & Hinton, G. E. 2012, in *Advances in Neural Information Processing Systems*, ed. F. Pereira, C. Burges, L. Bottou, & K. Weinberger, Vol. 25 (Curran Associates, Inc.). https://proceedings.neurips.cc/paper_files/paper/2012/file/c399862d3b9d6b76c8436e924a68c45b-Paper.pdf
- Li, J., Tenenbaum, P., Twicken, J. D., et al. 2019, *Publications of the Astronomical Society of the Pacific*, 131, 024506, doi: [10.1088/1538-3873/aaf44d](https://doi.org/10.1088/1538-3873/aaf44d)
- Lindgren, L., Klioner, S. A., Hernández, J., et al. 2021, *Astronomy & Astrophysics*, 649, A2, doi: [10.1051/0004-6361/202039709](https://doi.org/10.1051/0004-6361/202039709)
- Lomb, N. R. 1976, *Astrophysics and space science*, 39, 447
- Mandel, K., & Agol, E. 2002, *The Astrophysical Journal*, 580, L171–L175, doi: [10.1086/345520](https://doi.org/10.1086/345520)
- McCauliff, S. D., Jenkins, J. M., Catanzarite, J., et al. 2015, *The Astrophysical Journal*, 806, 6, doi: [10.1088/0004-637x/806/1/6](https://doi.org/10.1088/0004-637x/806/1/6)
- Morris, R. L., Twicken, J. D., Smith, J. C., et al. 2020, *Kepler Data Processing Handbook: Photometric Analysis*, Kepler Science Document KSCI-19081-003, id. 6. Edited by Jon M. Jenkins.
- Morton, T. D., Bryson, S. T., Coughlin, J. L., et al. 2016, *The Astrophysical Journal*, 822, 86, doi: [10.3847/0004-637x/822/2/86](https://doi.org/10.3847/0004-637x/822/2/86)
- Ng, A. Y. 2016, in *Advances in Neural Information Processing Systems (MIT Press)*. <https://media.nips.cc/Conferences/2016/Slides/6203-Slides.pdf>
- Osborn, H. P., Ansdell, M., Ioannou, Y., et al. 2020, *Astronomy & Astrophysics*, 633, A53, doi: [10.1051/0004-6361/201935345](https://doi.org/10.1051/0004-6361/201935345)
- Prša, A., Kochoska, A., Conroy, K. E., et al. 2022, *The Astrophysical Journal Supplement Series*, 258, 16, doi: [10.3847/1538-4365/ac324a](https://doi.org/10.3847/1538-4365/ac324a)
- Ricker, G. R., Winn, J. N., Vanderspek, R., et al. 2015, *Journal of Astronomical Telescopes, Instruments, and Systems*, 1, 014003, doi: [10.1117/1.JATIS.1.1.014003](https://doi.org/10.1117/1.JATIS.1.1.014003)
- Salinas, H., Pichara, K., Brahm, R., Pérez-Galarce, F., & Mery, D. 2023, *Monthly Notices of the Royal Astronomical Society*, 522, 3201–3216, doi: [10.1093/mnras/stad1173](https://doi.org/10.1093/mnras/stad1173)
- Savitzky, A., & Golay, M. J. E. 1964, *Analytical Chemistry*, 36, 1627, doi: [10.1021/ac60214a047](https://doi.org/10.1021/ac60214a047)
- Scargle, J. D. 1982, *Astrophysical Journal*, Part 1, vol. 263, Dec. 15, 1982, p. 835–853., 263, 835
- Schapire, R. E. 1990, *Machine Learning*, 5, 197, doi: [10.1007/BF00116037](https://doi.org/10.1007/BF00116037)
- Schmidhuber, J. 2022, *Annotated History of Modern AI and Deep Learning*. <https://arxiv.org/abs/2212.11279>
- Schwarz, G. 1978, *The annals of statistics*, 461
- Seader, S., Tenenbaum, P., Jenkins, J. M., & Burke, C. J. 2013, *ApJS*, 206, 25, doi: [10.1088/0067-0049/206/2/25](https://doi.org/10.1088/0067-0049/206/2/25)
- Seader, S., Jenkins, J. M., Tenenbaum, P., et al. 2015, *The Astrophysical Journal Supplement Series*, 217, 18, doi: [10.1088/0067-0049/217/1/18](https://doi.org/10.1088/0067-0049/217/1/18)
- Shallue, C. J., & Vanderburg, A. 2018, *The Astronomical Journal*, 155, 94
- Smith, J. C., Stumpe, M. C., Van Cleve, J. E., et al. 2012, *Publications of the Astronomical Society of the Pacific*, 124, 1000, doi: [10.1086/667697](https://doi.org/10.1086/667697)

- Stoica, P., & Selen, Y. 2004, IEEE Signal Processing Magazine, 21, 36, doi: [10.1109/MSP.2004.1311138](https://doi.org/10.1109/MSP.2004.1311138)
- Stumpe, M. C., Smith, J. C., Van Cleve, J. E., et al. 2012, Publications of the Astronomical Society of the Pacific, 124, 985–999, doi: [10.1086/667698](https://doi.org/10.1086/667698)
- Sullivan, P. W., Winn, J. N., Berta-Thompson, Z. K., et al. 2015, The Astrophysical Journal, 809, 77, doi: [10.1088/0004-637X/809/1/77](https://doi.org/10.1088/0004-637X/809/1/77)
- Tey, E., Moldovan, D., Kunimoto, M., et al. 2023, The Astronomical Journal, 165, 95, doi: [10.3847/1538-3881/acad85](https://doi.org/10.3847/1538-3881/acad85)
- Twicken, J. D., Caldwell, D. A., & et al. 2020, EXP-TESS-ARC-ICD-0014 Rev F. https://archive.stsci.edu/files/live/sites/mast/files/home/missions-and-data/active-missions/tess/_documents/EXP-TESS-ARC-ICD-TM-0014-Rev-F.pdf
- Twicken, J. D., Chandrasekaran, H., Jenkins, J. M., et al. 2010, in Software and Cyberinfrastructure for Astronomy, ed. N. M. Radziwill & A. Bridger, Vol. 7740, International Society for Optics and Photonics (SPIE), 77401U, doi: [10.1117/12.856798](https://doi.org/10.1117/12.856798)
- Twicken, J. D., Catanzarite, J. H., Clarke, B. D., et al. 2018a, Publications of the Astronomical Society of the Pacific, 130, 064502, doi: [10.1088/1538-3873/aab694](https://doi.org/10.1088/1538-3873/aab694)
- . 2018b, Publications of the Astronomical Society of the Pacific, 130, 064502, doi: [10.1088/1538-3873/aab694](https://doi.org/10.1088/1538-3873/aab694)
- Valizadegan, H., Martinho, M. J. S., Jenkins, J. M., et al. 2023, The Astronomical Journal, 166, 28, doi: [10.3847/1538-3881/acd344](https://doi.org/10.3847/1538-3881/acd344)
- Valizadegan, H., Martinho, M. J. S., Wilkens, L. S., et al. 2022, The Astrophysical Journal, 926, 120, doi: [10.3847/1538-4357/ac4399](https://doi.org/10.3847/1538-4357/ac4399)
- Van Cleve, J. E., & Caldwell, D. A. 2016, Kepler Instrument Handbook, Kepler Science Document KSCI-19033-002, id.1. Edited by Michael R. Haas and Steve B. Howell
- Vapnik, V. N. 1998, Statistical Learning Theory (Wiley-Interscience). <https://www.wiley.com/en-us/Statistical+Learning+Theory-p-9780471030034>
- Vaswani, A., Shazeer, N., Parmar, N., et al. 2023, Attention Is All You Need. <https://arxiv.org/abs/1706.03762>
- Yu, L., Vanderburg, A., Huang, C., et al. 2019, The Astronomical Journal, 158, 25, doi: [10.3847/1538-3881/ab21d6](https://doi.org/10.3847/1538-3881/ab21d6)

APPENDIX

A. DETAILS OF OPTIMIZED ARCHITECTURE FOR EXOMINER++

We provide in detail the architecture and optimization parameters of **ExoMiner++**:

- The ‘Difference Image’ branch has three convolutional blocks each with three convolutional layers. The three convolutional blocks have convolutional layers with 4, 8, and 16 filters, respectively. All convolutional layers have filters of size $3 \times 3 \times 1$ followed by a maxpooling layer with $2 \times 2 \times 1$.
- All other convolutional branches have two convolutional blocks each with three convolutional layers. The two convolutional blocks have convolutional layers with 8 and 16 filters, respectively. Transit-view convolutional branches have filters of size 6 and 4 for the convolutional and maxpooling layers, respectively. Full-orbit branches (and the ‘Periodogram’ branch) have filters of size 5 and 8 for the convolutional and maxpooling layers, respectively.
- All convolutional layers use ‘same’ padding (i.e., the feature map output is preserved), a stride of 1, and their weights are initialized randomly following He initialization (He et al. 2015). All maxpooling layers use ‘valid’ padding and a stride of 1.
- The Fully Connected (FC) layer at the end of each branch has 4 neurons and a dropout rate of 12.11% (applied only during training).
- The final FC block has four FC layers, each with 512 neurons and with a dropout rate of 2.15% (again, applied only during training).
- All convolutional and FC layers are followed by a rectified linear unit activation (Fukushima 1969, ReLU).
- Learning rate was set to $4.18e-5$.

Table 17. Hyperparameter Optimizer Parameters.

Parameter	Value(s)
Budget (number of training epochs)	6, 12, 25, 50
η	2
Top-n (%)	15
Random fraction	0.3
Number of samples	64
Bandwidth factor	3
Minimum bandwidth	0.001

Table 18. Values/ranges of tested hyperparameters for ExoMiner++. All hyperparameters are integers except for the learning rate and the dropout rate hyperparameters which are real values.

Hyperparameter	Range/Values
Learning rate	$[1e-6, 1e-1]$
Number of conv blocks (transit view)	$[1, 5]$
Number of conv blocks (full-orbit view)	$[1, 5]$
Number of conv layers per block	$[1, 3]$
Initial number of kernels	2^x for integer $x \in [2, 6]$
Kernel size (transit view)	$[1, 8]$
Kernel size (full-orbit view)	$[1, 8]$
Pool size (transit view)	2^x for integer $x \in [1, 4]$
Pool size (full-orbit view)	2^x for integer $x \in [1, 4]$
Number of FC neurons in conv branch FC layer	$[1, 4]$
Dropout rate for conv branch FC layer	$1e-3, 0.2$
Number of FC layers in FC block	$[1, 4]$
Number of neurons in FC block layers	2^x for integer $x \in [5, 9]$
Dropout rate for FC block layers	$1e-3, 0.2$